MASTER THESIS

Design Study of Radio Frequency Knockout Slow Extraction for the MedAustron Synchrotron

submitted to the Atominstitut of the Vienna University of Technology, 1040 Wien
in cooperation with MedAustron, 2700 Wiener Neustadt

under supervision of

Andrea DE FRANCO, PhD

and

Privatdoz. Dipl.-Ing. Dr.techn. Michael BENEDIKT

by

Florian Kühteubl
Matrikelnummer 01226869

Katzelsdorf, March 10, 2020

Florian Kühteubl

Abstract

MedAustron is a state-of-the-art ion therapy facility in Wiener Neustadt with the aim to treat cancer patients with ion beams. The extraction of the accelerated particles with the desired energy from the synchrotron to the treatment rooms is one of the critical steps of the process. A stable beam of five seconds with a constant intensity is mandatory to achieve high quality patient treatment. To reach such long extraction times, third order resonant slow extraction is used.
At MedAustron, slow extraction is currently driven by a betatron core, which increases the particle momentum to move the beam slowly into the resonance condition. However, current ripples on synchrotron components (especially quadrupoles) have got a negative impact on the quality of the extracted spill. Additionally, a fast change of the beam energy via multi energy extraction is not possible with betatron core driven extraction.
To address these problems, the slow extraction mechanism could be changed to a slow extraction driven by Radio Frequency Knockout (RF KO). This method increases the transverse amplitude of the particles by applying an RF voltage to a transverse kicker. The current is modulated with a frequency corresponding to the revolution frequency times the horizontal tune of the particles.

The design of such a mechanism is the goal of this Master thesis, which is undertaken by simulations of the extraction process with MAD-X and Python.
Firstly, the Steinbach diagram of the extraction is re-constructed via simulations and the behaviour under parameter variation is studied.
Secondly, the basic principle of RF KO is tested and the optimal choice of the lattice parameters such as horizontal tune Q_H and horizontal chromaticity Q'_H is determined in order to maximize beam intensity and quality after extraction.
Thirdly, promising candidates for RF KO are investigated more closely and a comparison to the betatron core-driven extraction is drawn.

Contents

1. Introduction **1**
- 1.1. The MedAustron accelerator complex . . . 1
- 1.2. Scope of the thesis . . . 3

2. Introduction to accelerator physics **5**
- 2.1. Particle motion in a circular accelerator . . . 5
  - 2.1.1. The transfer matrix . . . 7
  - 2.1.2. The Twiss functions . . . 9
  - 2.1.3. The concept of emittance . . . 10
  - 2.1.4. The motion of off-momentum particles . . . 12
- 2.2. The third-order resonant extraction . . . 13
  - 2.2.1. Kobayashi Hamiltonian and the stable triangle . . . 14
  - 2.2.2. The Hardt condition . . . 18
  - 2.2.3. Steinbach diagram . . . 20
  - 2.2.4. Extraction methods . . . 21

3. Preparatory simulations **25**
- 3.1. Construction of the Steinbach diagram . . . 25
  - 3.1.1. Chromaticity correction . . . 27
  - 3.1.2. Parameter scans . . . 31
- 3.2. Simulation of betatron core extraction . . . 34
  - 3.2.1. Creating the initial particle distribution . . . 34
  - 3.2.2. Results of the simulation . . . 37

4. Simulation of the Radio Frequency Knockout extraction **39**
- 4.1. The extraction diagram . . . 41
- 4.2. Proof of the Radio Frequency Knockout principle . . . 43
- 4.3. Scenarios for Radio Frequency Knockout . . . 45
  - 4.3.1. On-tune, off-momentum scenario . . . 45
  - 4.3.2. Off-tune, on-momentum scenario . . . 47
  - 4.3.3. Hybrid scenario . . . 49
- 4.4. Moving the electrostatic septum wall . . . 51

5. Promising candidates for Radio Frequency Knockout **53**
5.1. Knockout candidate 1 53
5.1.1. Comparison to betatron core extraction 56
5.1.2. Tracking to magnetostatic septum 59
5.1.3. Further tracking of the beamline 60
5.2. Knockout candidate 2 62

6. Summary and outlook **66**

A. Basis structure of the MAD-X scripts **76**

1. Introduction

In the following introductory chapter, the facility of MedAustron in general is described and an overview of the different parts of the accelerator complex is given. Additionally, the goal of the thesis is defined.

1.1. The MedAustron accelerator complex

MedAustron is a state-of-the-art facility for tumour therapy, located in Wiener Neustadt (Lower Austria). The patient is irradiated with high-energy protons or carbon ions. The energy of the particles is chosen accordingly to the desired penetration depth of the beam and ranges from 60 to 250 MeV for protons and 120 to 400 MeV for carbon ions.
To reach such energies, a particle accelerator is needed, which is realised as synchrotron at MedAustron. Dipoles bend the trajectory of the ion beam, while quadrupoles are used to focus the beam in either horizontal or vertical plane.[1]
The structure of the MedAustron particle accelerator is shown in Figure 1.1.

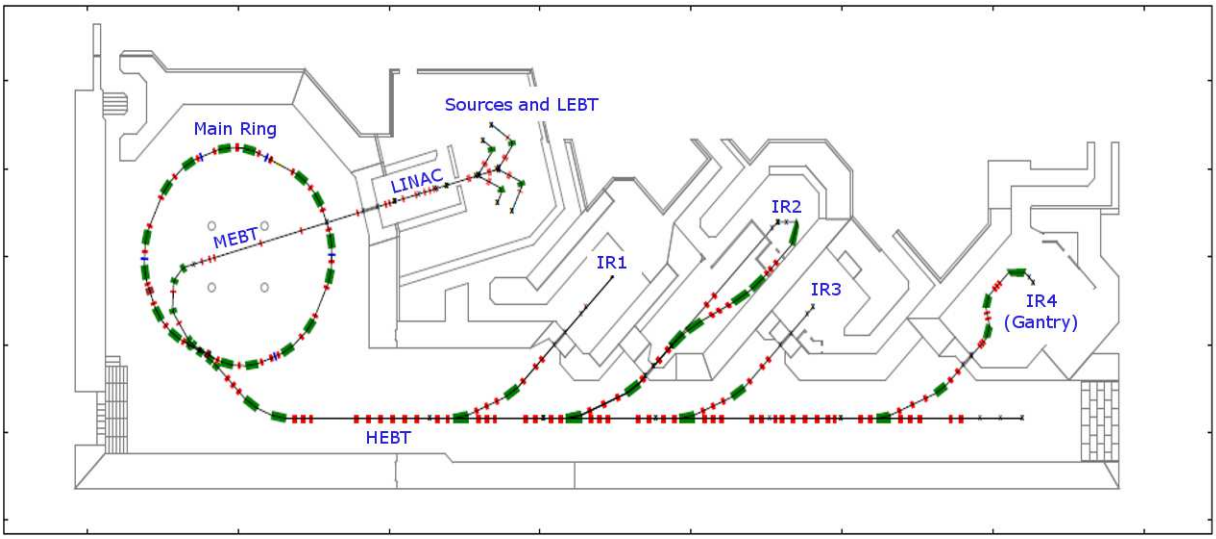

Figure 1.1.: The MedAustron accelerator complex (modified after [2])

The starting point of the accelerator chain is one of the three sources, where the ions are created by Electron Cyclotron Resonance (ECR). The first source produces hydrogen ions H_3^+ and the second carbon ions $^{12}C^{4+}$, while the third source is used as spare in case of a problem with one of the other sources and in preparation for future accelerator upgrades such as helium or oxygen beams
After extraction from the plasma chamber, the particles enter the Low Energy Beam Transfer Line (LEBT). A spectrometer magnet removes any unwanted particle types and quadrupoles focus the particle beam. Multiple beam instrumentation devices allow to analyse the properties of the beam such as position, intensity and beam profile.[3]

The first acceleration takes place in the linear accelerator (LINAC), where radio-frequent quadrupoles are used to accelerate the particles to an energy of 7 MeV/u. A stripping foil located at the end of the LINAC removes the remaining electrons from the ions, which transforms the hydrogen ions into three protons, while the carbon ions become $^{12}C^{6+}$.[4]
The LINAC is connected with the Main Ring via the Medium Energy Beam Transfer Line (MEBT). A debuncher cavity increases the bunch length and simultaneously reduces the momentum spread of the beam. Furthermore, a degrader is used to adjust the injected beam current. In normal clinical operation, degrader 20 is used for safety reasons, which means that only 20% of the initial current is transmitted to the Main Ring.[5]

The injection into the Main Ring (MR) is done via multiturn injection by filling the whole emittance of the MR. The MR is the main accelerator unit and is realised as a synchrotron, which means that the strengths of the dipoles and quadrupoles are increased during acceleration in synchronisation with the particle momentum, resulting in constant particle orbit during acceleration via RF cavity.[6]
At MedAustron, the beam is operated off-momentum, which means that the particle momentum is slightly smaller than the one of the reference particle. Shortly before extraction, a phase jump is performed to increase the momentum spread of the waiting beam to $\frac{\Delta p}{p} = 0.4\%$.
For sufficient medical treatment, a beam with a length of five seconds and constant intensity is required. To deliver such long beams, third-order resonant slow extraction is used. The on-momentum tune is set to resonance at $Q_H = 5/3$ and the resonant sextupole (MXR) is turned on. As the circulating beam is operated off-momentum, no particles are extracted yet.[4]
A betatron core then slowly drives the waiting beam into resonance by increasing the momentum. The amplitude of the now on-momentum particle grows bigger until it jumps on the other side of the electrostatic septum (ESE) wire and gets deflected by an electric field. After another deflection at the magnetostatic septum (MST), the particles leave the Main Ring.[4] The extraction process is explained more detailed in section 2.2.4.

After extraction from the Main Ring, the beam is guided to the treatment rooms through the High Energy Beam Transfer Line (HEBT). A magnetic chicane, referred to as chopper, is installed at the beginning of the HEBT, which is a safety measure to avoid unintentional irradiation. The spot size of the beam can be adjusted via a phase stepper, which rotates the beam in phase space, resulting in adjustable spot sizes between two and ten millimetre.[7]
MedAustron is equipped with four different irradiation rooms:

- IR1 is used only for non-clinical research.
- IR2 is used for patient treatment and is equipped with a horizontal and a vertical beamline.
- IR3 is equipped with a horizontal beamline for clinical use.
- IR4 is realized as a proton gantry, which can be rotated between $-30°$ and $+180°$ around the stationary patient to maximize treatment flexibility.

1.2. Scope of the thesis

The theoretical base of MedAustron is the Proton-Ion Medical Machine Study (PIMMS) Part I [8]. While MedAustron uses betatron core driven slow resonant extraction, most of the other medical facilities utilize radio frequency knockout (RF KO) to extract the particles from the synchrotron. For this method, which is further explained in section 2.2.4, a transverse kicker is used to excite the particles and push them into resonance.

The main advantages of using RF KO instead of betatron core driven extraction are described in the following enumeration.

1. **Multi energy extraction:**
   To irradiate tumour cells in different depths, it is necessary to adjust the beam energy accordingly. When the irradiation of the deepest layer is completed, the beam energy has to be decreased to treat layers closer to the surface. Thus, the particles in the Main Ring have to be de-accelerated.
   For betatron core extraction, a high momentum spread of the waiting beam is needed to allow the betatron core to push the particles fast into resonance. The momentum spread is increased prior to the extraction via a phase jump, which results in a coasting and thus de-bunched beam in the synchrotron.
   However, any changes of the beam energy requires to turn on the RF cavity again, for which a bunched beam is necessary. Because of this, a 're-bunching' is mandatory

to change the beam energy without dumping the beam. Unfortunately, the 're-bunching' is expected to lead to high particle losses. Therefore, the beam energy cannot be changed dynamically with betatron core extraction, the beam circulating in the Main Ring has to be dumped and a new acceleration cycle has to be started to irradiate with a different energy. This procedure results in a major time delay in the magnitude of a few seconds during patient treatment, which should be reduced in order to increase efficiency.
For RF KO, the momentum spread does not have to be enlarged and the mechanism is also compatible with bunched beams. Therefore, the energy of the circulating beam can be adapted during treatment and multi energy extraction is possible.[9]

2. **Dynamic intensity control:**
As the reaction of the betatron core is rather slow, it takes few tens of a millisecond to modulate the beam intensity.
In contrast, RF KO extraction allows a sub-millisecond adaptation of the beam intensity, paving the way for a dynamic intensity control during treatment via feedback loop to ensure that each spot is irradiated with the optimal intensity.[10]

3. **Irradiation gating:**
In addition to the dynamic intensity control, the extraction is immediately stopped when the RF voltage on the kicker is turned off. This enables treatment of organs which are affected by breathing movements, as the irradiation can be synchronised with the breathing process to assure a constant position of the tumour.[11]

4. **Ripple suppression:**
By advanced frequency modulation of the RF voltage applied on the transverse kicker, the ripples of the extracted spill can be considerably reduced. By adaptation of the excitation pattern, a better ripple suppression in comparison to betatron core extraction can be achieved.[12]
Additionally, low frequency ripples can be suppressed by a closed-loop feedback regulation on an intensity monitor.[10]

Due to these reasons, RF KO is a potentially promising alternative to betatron core extraction in order to minimize treatment duration and to extend the field of application of ion treatment at MedAustron.
The goal of this thesis is to study and simulate the feasibility of implementing RF KO at MedAustron and to analyse which parameter settings result in a satisfying extraction efficiency.

2. Introduction to accelerator physics

The aim of this chapter is to provide an overview of some selected topics of accelerator physics, which are relevant for the simulations presented in the next chapter. It must not be mistaken as a complete and rigorous introduction to the whole scientific field. For this, it can be referred to various accelerator physics books such as [13] and [14].
The discussed concepts and methods are utilised for synchrotrons in general and, in particular, for the MedAustron accelerator complex. A special attention is drawn to the third-order resonant slow extraction, as this process is widely used for clinical treatment of tumour patients with synchrotron based machines.

2.1. Particle motion in a circular accelerator

The source for the theoretical considerations of this section are the proceedings of the Fifth General Accelerator Physics Course at the CERN Accelerator School [15].

If a magnetic field B_0 is applied on a particle with charge q, mass m and velocity v, both centrifugal and Lorentz force affect the trajectory of the particle. When the two forces are equally strong, the resulting overall radial force disappears and the particle moves in a circle of radius ρ, which can be derived with equation 2.1.

$$\begin{aligned} \frac{mv^2}{\rho} &= qvB_0 \\ \rho &= \frac{mv}{qB_0} = \frac{p_0}{qB_0} \end{aligned} \tag{2.1}$$

A particle which follows this ideal circular trajectory is denoted as *reference particle*.
Any other particle with a small deviation from the ideal orbit either in horizontal (i.e. radial) or in vertical plane will start to oscillate around the reference particle, if restoring forces are present (by quadrupoles in both planes or by weak focusing of dipoles in horizontal plane). To derive a mathematical description of this oscillation is the key to understand the fundamental concepts of accelerator physics.

For the following derivation, a local cylindrical coordinate system (r, θ, z) as shown in Figure 2.1 is used, which follows the reference particle on the circular orbit at $z = 0$.

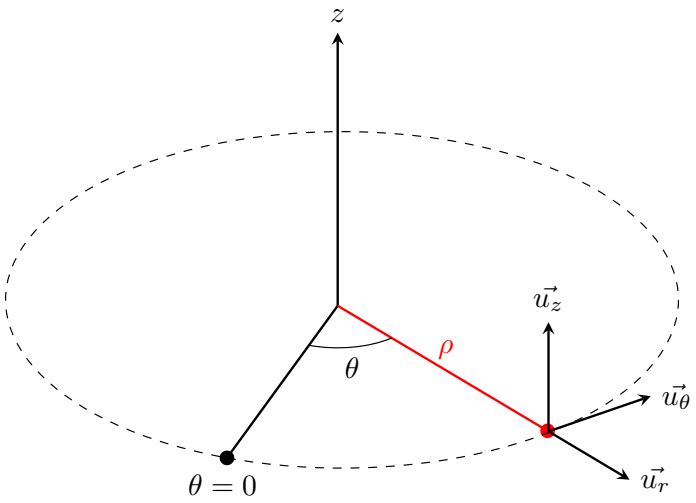

Figure 2.1.: Local cylindrical coordinate system

In this coordinate system, the particles are only affected by the Lorentz force, as the centrifugal force vanishes in the chosen system. The spatial components of the force are now written as vector in the base $\{\vec{u_r}, \vec{u_\theta}, \vec{u_z}\}$.

$$m\vec{a} = -q\vec{v} \times \vec{B} = -q \begin{pmatrix} \dot{r} \\ r\dot{\theta} \\ \dot{z} \end{pmatrix} \times \begin{pmatrix} B_r \\ B_\theta \\ B_z \end{pmatrix} \tag{2.2}$$

To study the effect of both dipoles and quadrupoles, the special case of a combined-function magnet is used to further simplify the equation of motion. The magnetic field of a combined-function magnet in cylindrical coordinates is given in equation 2.3.

$$\vec{B} = \vec{B}_{\text{dipole}} + \vec{B}_{\text{quadrupole}} = \begin{pmatrix} 0 \\ 0 \\ B_0 \end{pmatrix} + \begin{pmatrix} -gz \\ 0 \\ -gx \end{pmatrix} \tag{2.3}$$

B_0 and g are the dipole and the quadrupole strength of the magnet, respectively. With this linearisation of the magnetic field, effects of higher order cannot be studied. That means that the equations derived in this section cannot be used to investigate the effects of multipole magnets with a order higher than two (sextupoles, octupoles, ...).

After some further calculations and Taylor approximations of the small deviations from the reference orbit, the basic equations of transverse (i.e. radial and vertical) motion of a particle in a circular accelerator can be expressed.

$$x'' - \left(k - \frac{1}{\rho^2}\right) x = \frac{1}{\rho} \frac{\Delta p}{p_0} \tag{2.4}$$

$$z'' + kz = 0 \tag{2.5}$$

k is introduced as abbreviation for the term $\frac{qg}{p_0}$, which quantifies the focusing strength of the quadrupole component of the magnetic field. On the other hand, the bending radius of the dipole component of the magnetic field is denoted as ρ. The deviation of the particle momentum from the one of the reference particle is written as Δp.

The equations of motion for both planes can be written in the more general form

$$y'' + K(s)y = U(s) \tag{2.6}$$

with the abbreviations summarised in Table 2.1.

Table 2.1.: Abbreviations used for the general equation of motion for both planes

	y	$K(s)$	$U(s)$
radial motion	x	$-\left(k - \frac{1}{\rho^2}\right)$	$\frac{1}{\rho}\frac{\Delta p}{p_0}$
vertical motion	z	k	0

2.1.1. The transfer matrix

The solution of the equation of motion in horizontal plane is a linear transformation of the initial particle coordinates in phase space (x, x'), which can be written in one combined matrix equation 2.7.

$$\begin{pmatrix} x(s) \\ x'(s) \end{pmatrix} = \begin{pmatrix} C & S \\ C' & S' \end{pmatrix} \begin{pmatrix} x_0 \\ x'_0 \end{pmatrix} + \frac{\Delta p}{p} \begin{pmatrix} D \\ D' \end{pmatrix} \tag{2.7}$$

$C(s)$ and $S(s)$ are linear independent *mapping functions*, which map the initial particle coordinates (x_0, x'_0) to the particle coordinates at a certain distance s.

$$x(s) = C(s)x_0 + S(s)x'_0 \tag{2.8}$$

Both mapping functions can be calculated from the function $K(s)$.

The *dispersion vector* $(D(s), D'(s))$ originates from the inhomogeneous part of the equation of motion and adds an additional offset to the particle coordinates as defined in equation 2.9.

$$\begin{pmatrix} \Delta x(s) \\ \Delta x'(s) \end{pmatrix} = \begin{pmatrix} D(s) \\ D'(s) \end{pmatrix} \frac{\Delta p}{p_0} \tag{2.9}$$

The advantage of this matrix formalism is that adding multiple elements to a lattice translates to a simple matrix multiplication of the corresponding transfer matrices of each of the components.

A more compact version of equation 2.7 uses a 3x3 matrix to account also the dispersive effect on the particle trajectory in a single matrix equation 2.10. It adds the momentum offset as third variable to the phase space coordinates.

$$\begin{pmatrix} x(s) \\ x'(s) \\ \frac{\Delta p}{p} \end{pmatrix} = \begin{pmatrix} C & S & D \\ C' & S' & D' \\ 0 & 0 & 1 \end{pmatrix} \begin{pmatrix} x_0 \\ x'_0 \\ \frac{\Delta p}{p} \end{pmatrix} \tag{2.10}$$

Equations 2.7 and 2.10 also describe the particle trajectory in vertical plane, when the definition for the 'vertical $K(s)$' is used to calculate the mapping functions $C(s)$ and $S(s)$. Additionally, it has to be taken into account that the inhomogeneous term is missing for the vertical equation of motion 2.5, which means that the dispersion vector is zero for all magnetic elements.

For the case that $K(s)$ is constant with respect to s (or at least piecewise constant), the differential equations are solved analytically with a sine and a cosine approach, which can be easily confirmed by inserting the solution in the differential equation. The integration constants can evaluated from the initial conditions for $C(s)$ and $S(s)$ at $s = 0$.

$$\begin{aligned} C(s) &= \cos(\sqrt{K}s) \\ S(s) &= \frac{1}{\sqrt{K}} \sin(\sqrt{K}s) \end{aligned} \tag{2.11}$$

With this solution of the mapping function inserted in the matrix equation 2.10, the general homogeneous solution for an element with a piecewise constant function $K(s)$ can be expressed.

$$\begin{pmatrix} x_h(s) \\ x'_h(s) \end{pmatrix} = \begin{pmatrix} \cos(\sqrt{K}s) & \frac{1}{\sqrt{K}} \sin(\sqrt{K}s) \\ -\sqrt{K} \sin(\sqrt{K}s) & \cos(\sqrt{K}s) \end{pmatrix} \begin{pmatrix} x_0 \\ x'_0 \end{pmatrix} \tag{2.12}$$

2.1.2. The Twiss functions

For a circular accelerator, the periodicity of the lattices can be used as boundary condition. As $k(s)$ and $\rho(s)$ are periodic functions, also $K(s)$ is periodic with a period denoted as L.

$$K(s+L) = K(s) \tag{2.13}$$

If the circular accelerator with circumference C is composed of N identical sections, the length of such a section and thus the period length L can be calculated as $L = \frac{C}{N}$.

The on-momentum equation of motion $y'' + K(s)y = 0$ together with the periodicity condition 2.13 is called the *Hill's equation* and is the base for describing particle motion in a periodic lattice.
As shown in the previous section, the solution of the equation can be written as a general matrix equation with the transfer matrix $M(s)$.

$$\begin{pmatrix} x(s) \\ x'(s) \end{pmatrix} = M(s) \begin{pmatrix} x_0 \\ x'_0 \end{pmatrix} = \begin{pmatrix} C & S \\ C' & S' \end{pmatrix} \begin{pmatrix} x_0 \\ x'_0 \end{pmatrix} \tag{2.14}$$

If $K(s)$ is piecewise constant, the transfer matrix can be expressed as 'Twiss matrix'.

$$M(s) = \begin{pmatrix} 1 & 0 \\ 0 & 1 \end{pmatrix} \cos(\mu) + \begin{pmatrix} \alpha(s) & \beta(s) \\ -\gamma(s) & -\alpha(s) \end{pmatrix} \sin(\mu) \tag{2.15}$$

This new parametrisation originates from solving the Eigenwert problem of the transfer matrix.
$\alpha(s)$, $\beta(s)$ and $\gamma(s)$ are the so called *Twiss functions* and are periodic functions with a period of L.
μ denotes the phase of the particle and is independent of the position s in the accelerator lattice.

As the particle motion through the accelerator is symplectic, the determinant of the transfer matrix has to be 1. This condition leads to an important correlation between the Twiss parameter.

$$\beta\gamma - \alpha^2 = 1 \tag{2.16}$$

Further derivation and comparison with Hill's equation leads to another relation.

$$\alpha(s) = -\frac{1}{2}\beta'(s) \tag{2.17}$$

With this Twiss parametrisation, the solution of the Hill's equation can be written as a complex exponential function.

$$y_{1,2}(s) = a\sqrt{\beta(s)}e^{\pm i\Phi(s)} \tag{2.18}$$

Equation 2.18 shows that the amplitude of the particle motion is proportional to the square root of the beta function.
$\Phi(s)$ is the phase function, which is strongly linked to the phase advance μ per period L, which can be calculated by integrating the inverse of the beta function.

$$\mu = \int_s^{s+L} \frac{dt}{\beta(t)} \tag{2.19}$$

Another important parameter is the *tune* Q, which is defined as number of oscillations per revolution. As the accelerator is composed of N sections, the phase advance after one turn is $N\mu$. One oscillation corresponds to a phase advance of 2π. The tune can therefore be calculated by dividing the phase advance after one turn by 2π.

$$Q = \frac{N\mu}{2\pi} = \frac{1}{2\pi}\int_C \frac{ds}{\beta(s)} \tag{2.20}$$

The tune is an important parameter for the extraction process as it defines the impact of small field errors of the different magnetic components on the particle trajectory (see section 2.2).

2.1.3. The concept of emittance

The particle position is the real part of the solution of Hill's equation 2.18.

$$y(s) = a\sqrt{\beta(s)}\cos(\Phi(s) - \delta) \tag{2.21}$$

δ is an arbitrary, but constant phase. Differentiation and using correlation 2.17 leads to an expression for the particle angle y'.

$$y'(s) = -\frac{a}{\sqrt{\beta(s)}}\left(\sin(\Phi(s) - \delta) + \alpha(s)\cos(\Phi(s) - \delta)\right) \tag{2.22}$$

Equations 2.21 and 2.22 together describe an ellipse in phase space (x, x') of the area πa^2. When the phase space is observed at one fixed location and the position as well as the angle is recorded for one particle every turn, the ellipse is also continuously formed.
This can be explained by the fact that the particle performs Q oscillations per turn and

thus adds a constant phase to $\Phi(s)$ each turn, which can be viewed as a constant turn-by-turn increase of δ. When the tune is irrational, all points of the ellipse borderline are covered over time. However, if the tune is a rational number, the particles come back to the original position in phase space after a certain number of turns. If for example $Q = \frac{5}{3}$, a particle returns to its initial position after every three turns.

The cartesian coordinate representation of the phase space ellipse can be calculated from the parametric expressions 2.21 and 2.22.

$$\gamma y^2 + 2\alpha y y' + \beta y'^2 = a^2 \tag{2.23}$$

According the Liouville's theorem, the phase space density is invariant and thus constant, if the momentum of the particles is not changed. As a consequence, the area of the ellipse in phase space remains unchanged during revolution at constant momentum. This means that the left side of 2.23 is constant and denoted as *Courant-Snyder invariant*.
As the constant area of the ellipse plays an important role in accelerator physics, a new parameter is introduced, namely the *emittance* ϵ. The emittance replaces the formerly used expression a^2, which means that the area of the ellipse in phase space is therefore $\pi\epsilon$. If non-conservative forces like during the acceleration process are included, the emittance is no longer constant, but decreases during acceleration due to adiabatic dumping. To still have an invariant parameter, a normalization with respect to the particle momentum has to be done. The resulting *normalized emittance* ϵ_n is an invariant quantity during the whole acceleration process.

$$\epsilon_n = \left(\frac{p_0}{m_0 c}\right)\epsilon \tag{2.24}$$

The Twiss parameter determine the shape of the phase space ellipse, as shown in Figure 2.2.
The beam envelope $E(s)$ is defined as the maximum position and depends on the emittance and the beta function at a given location.

$$E(s) = \sqrt{\epsilon}\sqrt{\beta(s)} \tag{2.25}$$

The beam divergence $A(s)$ is the maximum of the angle function 2.22 and is determined by the emittance and the gamma function.

$$A(s) = \sqrt{\epsilon}\sqrt{\gamma(s)} \tag{2.26}$$

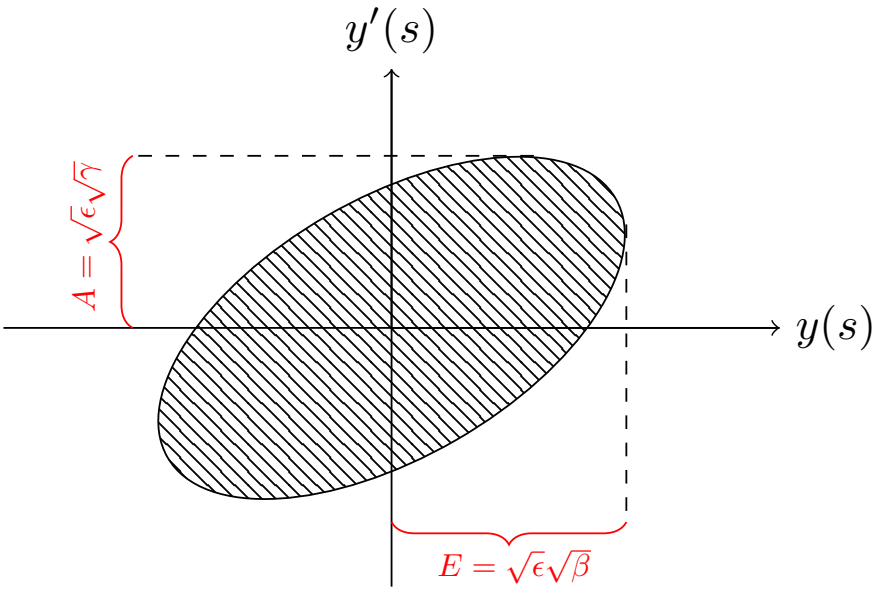

Figure 2.2.: The shape of the phase space ellipse, depending on the Twiss parameter

2.1.4. The motion of off-momentum particles

In the last section, the motion of on-momentum particles with $\frac{\Delta p}{p} = 0$ was discussed. If a momentum offset is introduced, two important effects arise.

1. As particles with a different momentum than the reference particle are deflected differently by the lattice dipoles, the ellipse is shifted in phase space for an off-momentum particle. The amplitude of this shifting is determined by the dispersion vector at a given position s.

$$\begin{pmatrix} \Delta x(s) \\ \Delta x'(s) \end{pmatrix} = \begin{pmatrix} D(s) \\ D'(s) \end{pmatrix} \frac{\Delta p}{p} \tag{2.27}$$

2. Off-momentum particles are focused differently by quadrupoles. This altered focal length also changes the tune 'felt' by the off-momentum particle. The proportional quantity between momentum offset and tune change is called *chromaticity* Q'.

$$\Delta Q = Q' \frac{\Delta p}{p} \tag{2.28}$$

2.2. The third-order resonant extraction

The Proton-Ion Medical Machine Study (PIMMS) Part I [8] is used as source for this section.

As described in the last section, the tune Q describes the number of oscillations per turn. If the tune is an integer, the particle returns to its initial position every turn. Small errors in the dipole field thus affect the particles always at the same position and increase the oscillation amplitude, until the particle hits the aperture and is lost.
Analogously, quadrupole field errors lead to resonances for half-integer tunes, while errors in the sextupole field excite resonances for third-integer tunes. Additionally, sextupoles and magnet misalignments lead to a coupling of the horizontal and vertical oscillation, which introduces coupled resonances for horizontal and vertical tune settings.
In general, a resonance of $(m+n)$th order can be defined as

$$mQ_x + nQ_z = l \qquad m, n, l \in \mathbb{N}. \tag{2.29}$$

Figure 2.3 shows a resonance diagram with all 'forbidden' resonances up to third order. For operating a particle accelerator, the working point (Q_x, Q_z) must not be chosen directly on any resonance line to avoid losses.[15]

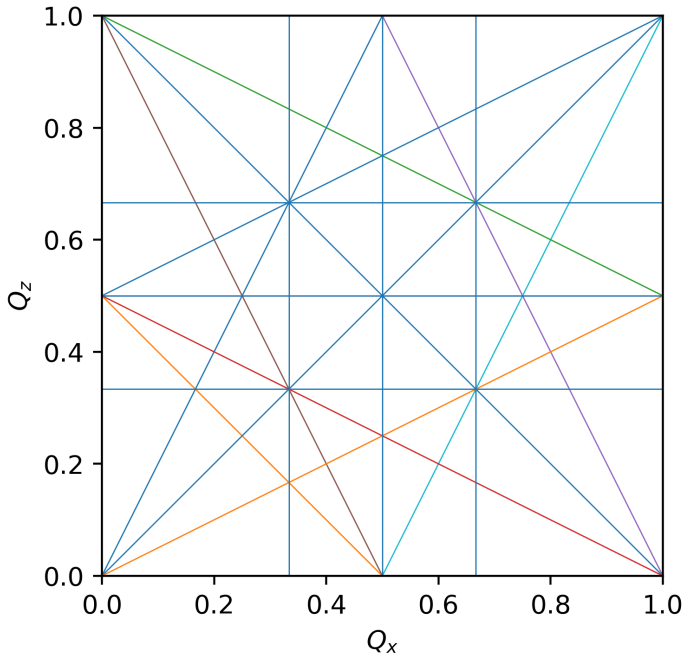

Figure 2.3.: Resonance diagram with resonances up to third order

However, resonances can also be utilized for slowly extracting the particles. Especially third-order resonances are suitable to control the extraction. For this, the working point is set near a resonance during acceleration and the waiting beam is than slowly driven into the resonance for extraction. The possibilities how to execute this process are discussed in section 2.2.4.

2.2.1. Kobayashi Hamiltonian and the stable triangle

To describe the particle motion in phase space close to a third-order resonance and including the effects of a resonant sextupole (with normalised sextupole strength S), the Kobayashi Hamiltonian 2.30 can be used. A step-by-step derivation of the Hamiltonian is provided in [8].

$$\mathbf{H} = \frac{\epsilon}{2}\left(X^2 + X'^2\right) + \frac{S}{4}\left(3XX'^2 - X^3\right) \tag{2.30}$$

In equation 2.30, ϵ is the *modified tune distance* defined as $\epsilon = 6\pi \cdot \delta Q$, with $\delta Q = Q - Q_{\text{res}}$ denoting the *tune distance* of the particle to the tune of the resonance.

The Kobayashi Hamiltonian is composed of two different terms, the unperturbed and the sextupole component.
The first is independent of the sextupole strength and proportional to the modified tune distance ϵ. Geometrically, it describes a circle in phase space with a radius $r = \sqrt{\frac{2\mathbf{H}}{\epsilon}}$, as shown on the left side of Figure 2.4.
The latter characterizes the effect of the resonant sextupole by dividing the phase space into six sectors, which represent the six poles of the magnet. A contour plot of the sextupole component is shown on the right side of Figure 2.4.

The contour plot of the whole Kobayashi Hamiltonian as superposition of the unperturbed and the sextupole component is shown in Figure 2.5. For small amplitudes, closed triangular trajectories are observed. Particles in this region follow the triangles and are thus stable.
However, if the particle amplitude exceeds a certain limit, the triangles break into opened trajectories, which means that the particles increase their amplitudes further and become unstable. This instability is used to extract the particles from the accelerator.
The boundaries between the stable triangles and the unstable area define the *separatrices*, which are shown as red lines in Figure 2.5.

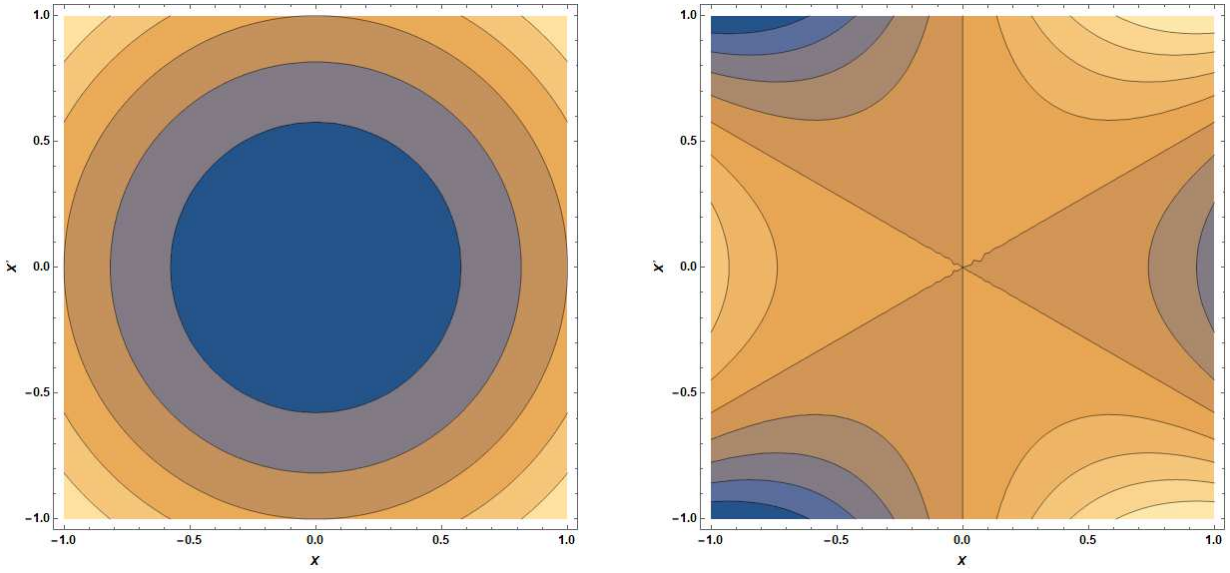

Figure 2.4.: Contour plot of the unperturbed circular (left) and the superimposed sextupole (right) component of the Kobayashi Hamiltonian 2.30

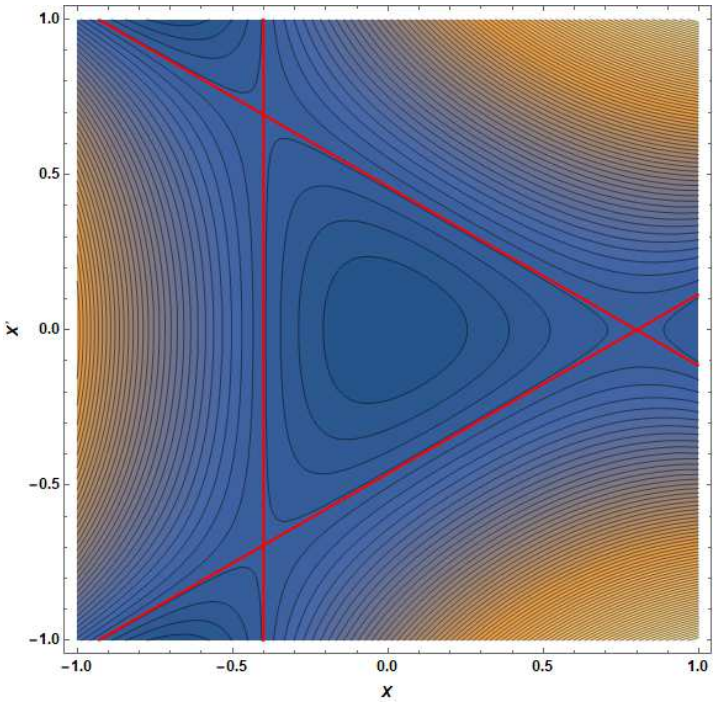

Figure 2.5.: Contour plot of the Kobayashi Hamiltonian 2.30 with separatrices (red)

Further analysis shows that the transition between stable and unstable area takes place at a certain value of the Hamiltonian.

$$H_{\text{separatrix}} = \frac{\left(\frac{2\epsilon}{3}\right)^3}{S^2} \tag{2.31}$$

At this value, the Kobayashi Hamiltonian can be factorised into three lines, which are the mathematical representation of the separatrices.

$$\left(\frac{S}{4}X + \frac{\epsilon}{6}\right)\left(\sqrt{3}X' + X - \frac{4\epsilon}{3S}\right)\left(\sqrt{3}X' - X + \frac{4\epsilon}{3S}\right) = 0 \tag{2.32}$$

The intersection of the separatrices together with the origin of the coordinate system define four fixed points of the Hamiltonian, which are the vertices and the center of the stable triangle. In the following, the abbreviation $h = \frac{2}{3}\frac{\epsilon}{S} = \frac{4\pi}{S}\delta Q$ is used to simplify the coordinates of the fixed points in phase space. The stable triangle and the coordinates of the fixed points P_0 to P_3 are shown in Figure 2.6.

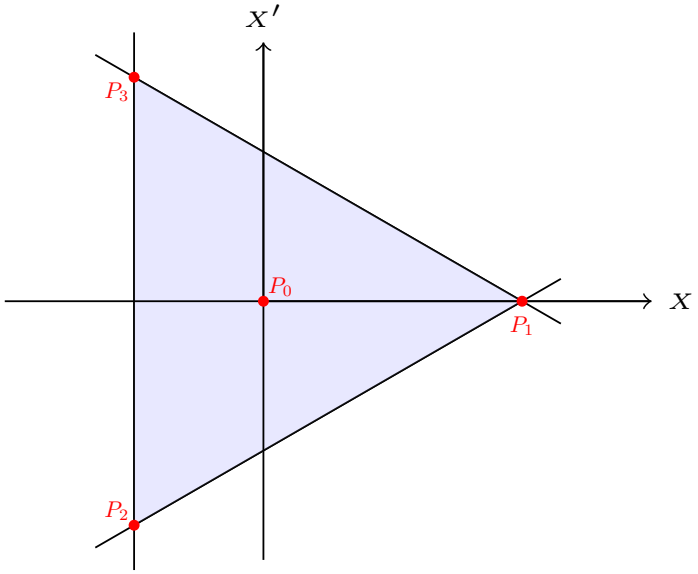

Point	Coordinates (X, X')
P_0	$(0, 0)$
P_1	$(2h, 0)$
P_2	$\left(-h, -\sqrt{3}h\right)$
P_3	$\left(-h, \sqrt{3}h\right)$

Figure 2.6.: The stable triangle at the resonant sextupole and the coordinates of the four fixed points

The area of the stable triangle, which is also referred to as *acceptance*, can be calculated via equation 2.33.

$$A_{\text{stable}} = \frac{3h \cdot 2\sqrt{3}h}{2} = 3\sqrt{3}h^2 = \frac{48\sqrt{3}\pi^2}{S^2}(\delta Q)^2 \tag{2.33}$$

The acceptance is proportional to the square of the ratio $\frac{\delta Q}{S}$, which means that the stable triangle shrinks the closer to resonance the tune is. The acceptance becomes zero directly at the resonant tune and all particles are unstable, independent of their amplitude.

If the dispersion is not equal to zero, the center of the triangle is shifted in direction of the local dispersion vector according to equation 2.27. This shifting has to be taken into account for off-momentum particles.

Until now, the stable triangle was only drawn at the position of the resonant sextupole. It can be shown that the shape of the triangle at any other position of the lattice can be computed by rotating the triangle around the center point P_0 by an angle defined by the phase advance between the resonant sextupole and the component of interest.
For example, the phase advance between the resonant sextupole and the electrostatic septum for the MedAustron lattice is designed as $\Delta\mu = 227.75°$.[6] Therefore, the original stable triangle at the MXR has to be rotated by this value to get the stable triangle at the ESE, as shown in Figure 2.7.
Additionally, the shift due to the new local dispersion vector at the position s has to be considered to calculate the actual stable triangle at any position.

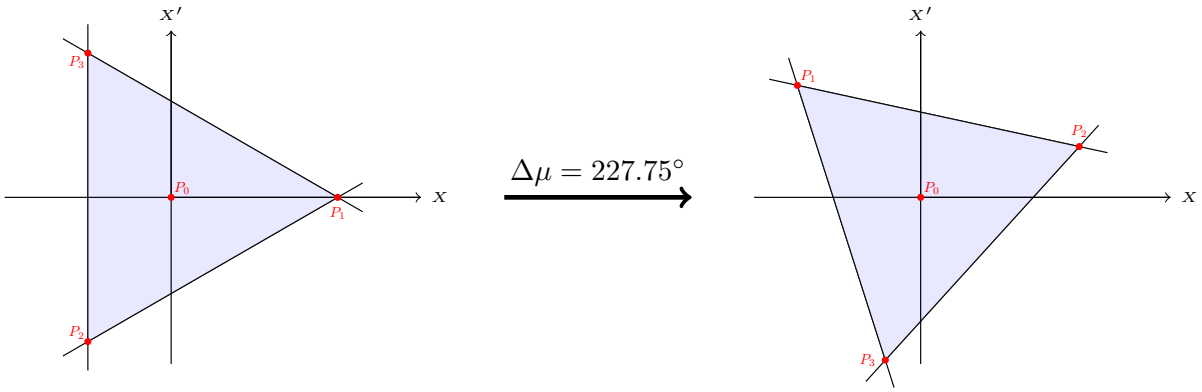

Figure 2.7.: The rotation of the separatrix in phase space from the resonant sextupole (*left*) to the electrostatic septum (*right*)

2.2.2. The Hardt condition

According to equation 2.33, the area of the stable triangle is proportional to the square of the tune distance and thus to the square of the momentum offset. The smaller the momentum offset of a particle is, the smaller gets the stable triangle. Because of this, the particles in a beam with a non-zero momentum spread are extracted along separatrices originating from stable triangles of different sizes, as shown for three particles with different momentum offsets in Figure 2.8.

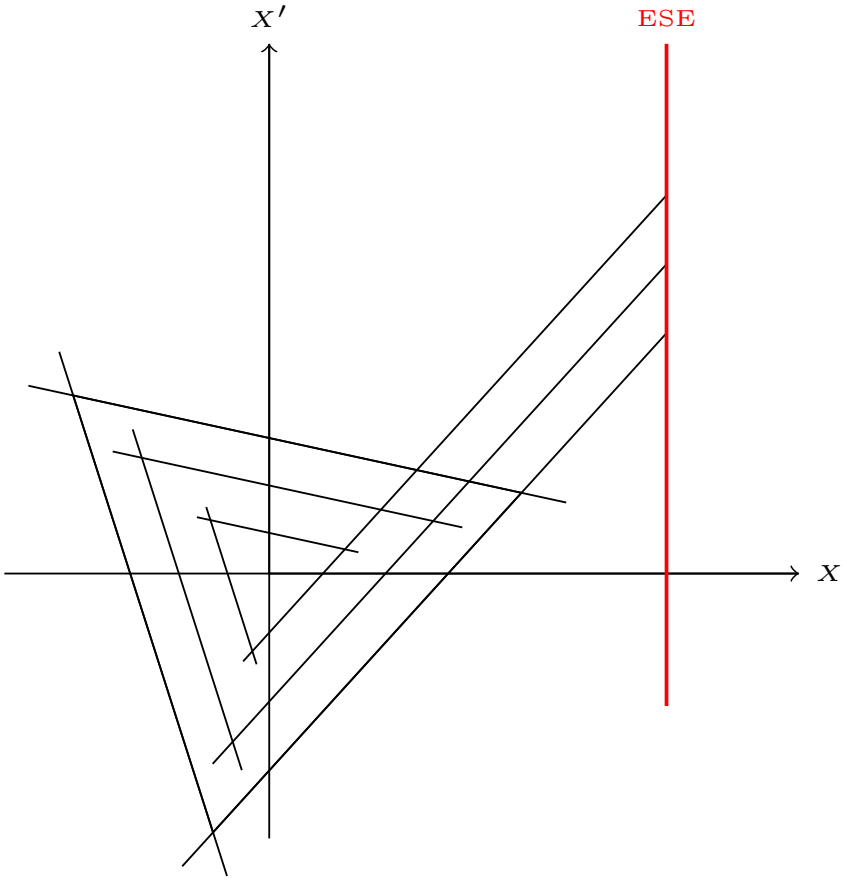

Figure 2.8.: Separatrices for three particles with different momentum offsets

One sees that the separatrices for different momenta are shifted. The particles thus reach the electrostatic septum wire at different angles X'. This can be a problem as the different entrance angles might lead to particles hitting the ESE wall somewhere along the length of the septum, which decreases the extraction efficiency.[8]

This problem can be solved by taking into account that the dispersion vector shifts the center of the stable triangle in dependence of the particle momentum. When the parameter are chosen accordingly, the separatrices for different momentum offsets can be superimposed by using the dispersive shifting, resulting in all particles independent of their momentum hitting the ESE wire with the same angle and a maximised extraction efficiency. This superposition is shown in Figure 2.9 for particles with a negative momentum offset, which means that the dispersion vector points in the opposite direction of the resulting shifting.

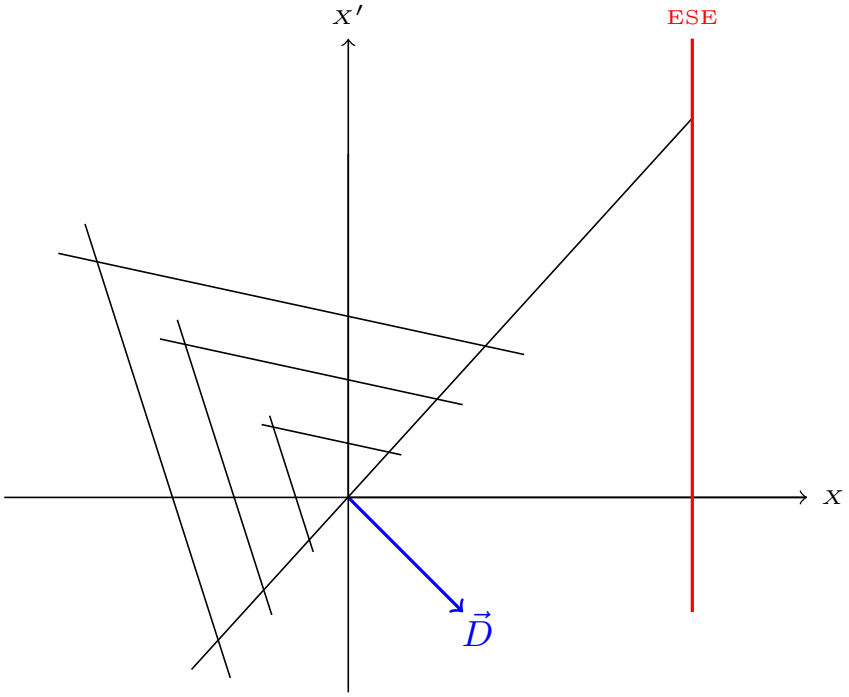

Figure 2.9.: Superimposed separatrices for particles with different $\frac{\Delta p}{p} < 0$

The requirement on the lattice functions for this superposition of the separatrices is called the *Hardt condition*[16].

$$D_n \cos(\alpha - \Delta\mu) - D'_n \sin(\alpha - \Delta\mu) = -\frac{4\pi}{S} Q' \tag{2.34}$$

Equation 2.34 connects the normalized dispersion vector (D_n, D'_n), the separatrix orientation at the resonant sextupole α and the phase advance between sextupole and ESE $\Delta\mu$ with the strength of the resonant sextupole S and the chromaticity Q'. The left side of equation is determined by the lattice design and the geometry of extraction, while S is also fixed by the spiral step. The only free parameter is the chromaticity Q', which can be varied to fulfil the Hardt condition.[8]

2.2.3. Steinbach diagram

Beside the phase space formalism discussed in the last section, another perspective on the process of resonant particle extraction is important. This time, the process is viewed in amplitude-momentum space and the resulting plot is called *Steinbach diagram*[8][17], as exemplary showed in Figure 2.10. The particle amplitude is defined as $A = \sqrt{\frac{E}{\pi}}$, with E denoting the single-particle emittance[1].
The abscissa is the momentum offset $\frac{\Delta p}{p}$ with respect to the reference particle, which corresponds to the tune offset for a constant chromaticity.
In this amplitude-momentum space, a 'V'-shaped unstable area appears near a resonance. The center of the 'V' is the resonant tune Q_{res}. The stable triangle for particles directly on this resonant tune vanishes and particles with all amplitudes are unstable. If a momentum offset is added to this resonant tune, the area of the stable triangle increases and particles with small amplitudes are still stable. As soon as the amplitude exceeds a certain limit, the stable triangle in phase space is left and the particle becomes unstable. This consideration explains the occurrence of the 'V'-shaped unstable region in amplitude-momentum space.

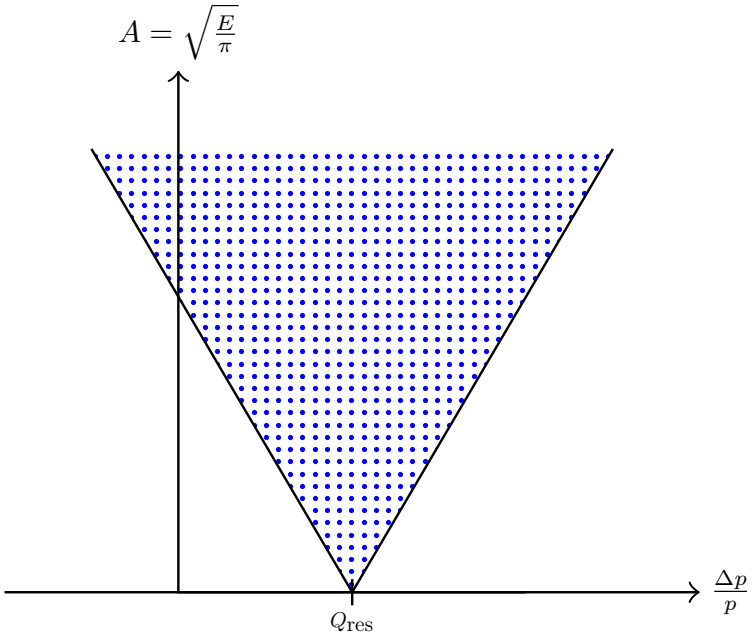

Figure 2.10.: Steinbach diagram near a resonant tune Q_{res}

[1]The single particle emittance can be calculated as $E = X^2 + X'^2$ from the normalised phase space coordinates of the particle.

To calculate the largest stable particle amplitude in dependence of the tune distance to resonance and thus the equation of the edge of the Steinbach diagram, equation 2.33 for the area of the stable triangle can be used.

$$A_{\text{lim}} = \sqrt{\frac{E_{\text{stable}}}{\pi}} = \sqrt{48\sqrt{3}\pi}\frac{\frac{\Delta p}{p} \cdot Q'_x}{|S|} \propto \frac{\delta Q_x}{|S|} \tag{2.35}$$

The amplitude limit is proportional to the tune distance to resonance (and thus to the momentum offset and the chromaticity value) and inverse proportional to the strength of the resonant sextupole.
After solving 2.35 towards δQ, the width of the 'V'-shape of the Steinbach diagram (also known as *stopband*) at a given single-particle emittance can be expressed. This results in a restriction on the particle tune for being in the unstable area and thus extracting the particle.

$$Q_{\text{res}} - \sqrt{\frac{1}{48\pi\sqrt{3}}\frac{E_{\text{stable}}}{\pi}}|S| < Q_{\text{particle}} < Q_{\text{res}} + \sqrt{\frac{1}{48\pi\sqrt{3}}\frac{E_{\text{stable}}}{\pi}}|S| \tag{2.36}$$

2.2.4. Extraction methods

To extract a particle, its tune has to be moved into the amplitude-dependent stopband defined in 2.36. There are multiple methods available for this process. The two extraction methods relevant for this thesis are presented in this section.

Betatron core driven extraction

This method is currently used at the MedAustron synchrotron. The circulating beam is operated off-momentum, which means that the central momentum of the particle distribution is not zero. After accelerating the beam, the on-momentum tune is set on a third-order resonance and the resonant sextupole is ramped. A betatron core inductively accelerates the waiting beam slowly into the stationary resonance by increasing the momentum and moving the particles from off- to on-momentum. As soon as a particle hits the stopband of the Steinbach diagram, its amplitude is increased and it is extracted. This momentum-selection process is visualized in Figure 2.11.

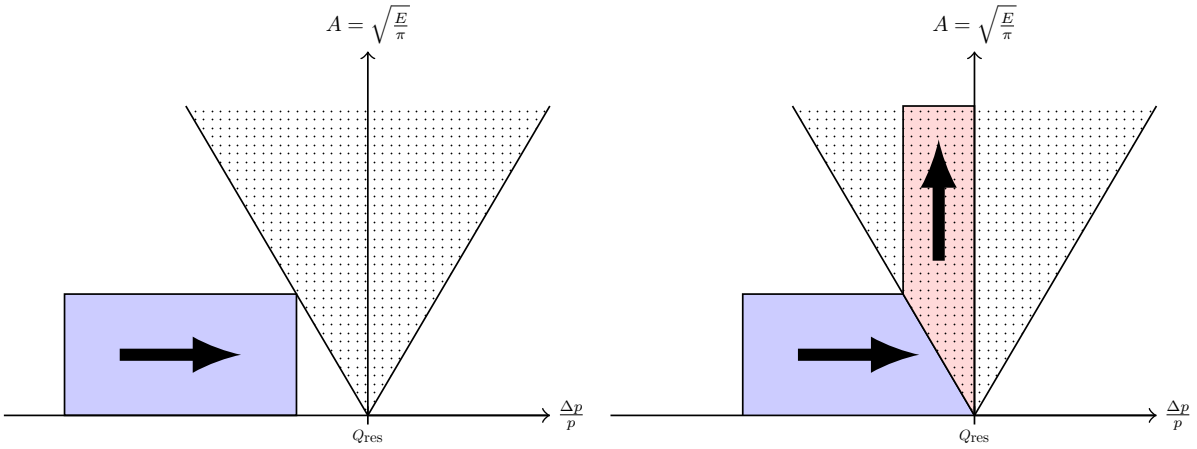

Figure 2.11.: Steinbach diagram for betatron core driven extraction

The results of simulating the phase space during extraction with MADX is visualised at the electrostatic septum in Figure 2.12. As the betatron core moves the particle from off- to on-momentum, the position approaches zero due to dispersion. Additionally, the triangular shape described above evolves when the particle is near resonance. As soon as the stopband is hit, the closed trajectory breaks open and the particle follows the separatrix until it is extracted at the ESE.

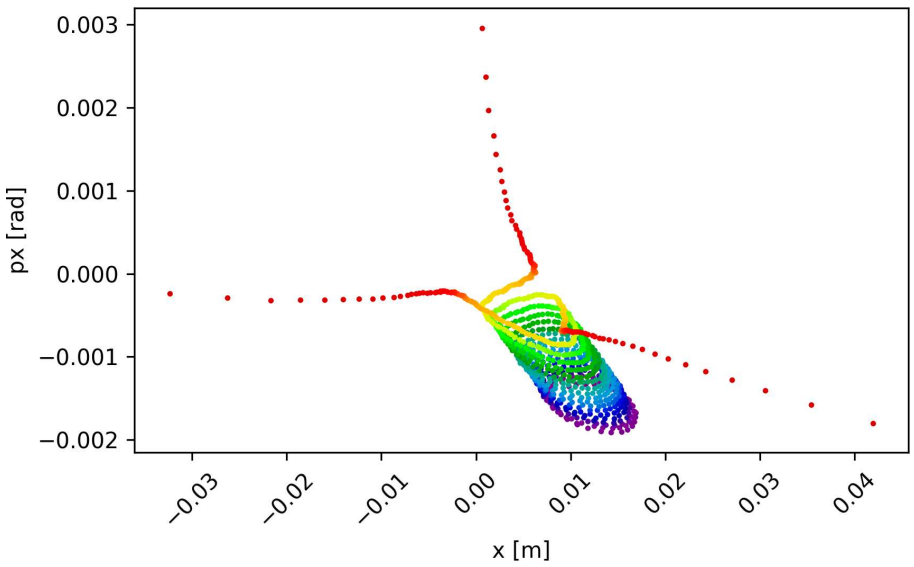

Figure 2.12.: Single particle phase space for betatron core driven extraction with colour-coded turn number[18]

For betatron core extraction, some considerations about the parameter choice have to be taken into account.

1. The wider the momentum spread of the waiting beam, the longer takes the extraction process for the same betatron core voltage. Additionally, a flat distribution in momentum space of the waiting beam is preferred to yield a constant intensity time profile of the extracted beam.

2. The emittance of the waiting beam should be small, so that the particles do not hit the stopband too early.

3. The momentum distribution of the extracted beam depends on the slope of the Steinbach diagram and thus on the chromaticity. A high chromaticity should be used to get a small momentum spread in the extracted beam.
   The chromaticity is also an important variable to fulfil the Hardt condition 2.34 in order to maximise extraction efficiency.

Radio frequency knockout (RF KO) driven extraction

The second method important for this thesis is the radio frequency knockout approach. The beam with a small momentum spread is operated near a third-order resonance. Different to the betatron core driven extraction discussed before, the particle momentum remains unchanged, but the transverse amplitude is increased until the particle hits the unstable area of the Steinbach diagram. The beam is therefore transversally excited and the extraction is based on amplitude selection, as shown in Figure 3.7.

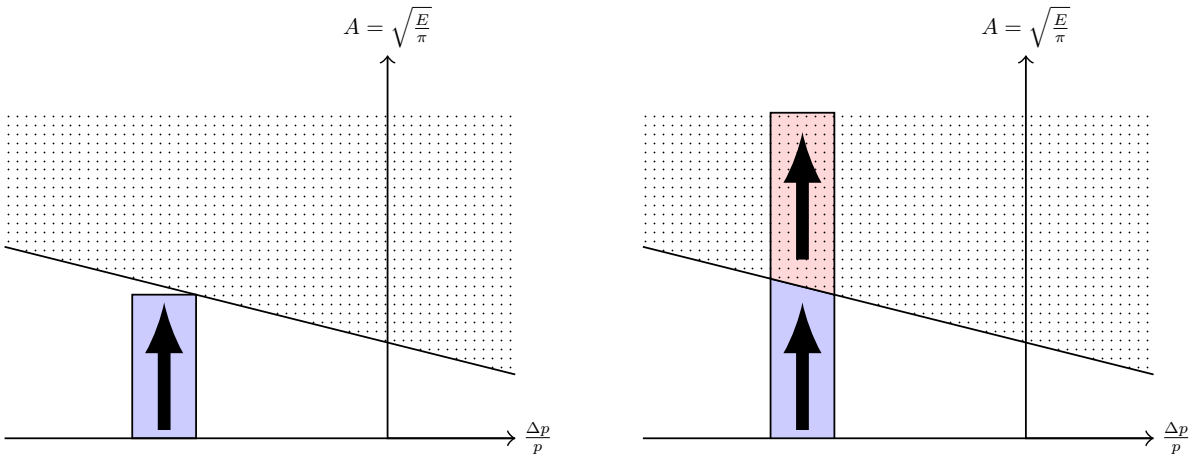

Figure 2.13.: Steinbach diagram for RF knockout driven extraction

For this transverse excitation, a horizontal kicker is fed with radio frequency current to blow up the horizontal emittance. To resonantly increase the particle amplitude, the frequency of this alternating current has to be matched with the horizontal particle tune. More precisely, it must be an integer multiple of the revolution frequency f_{rev} times the fractional part of the horizontal tune q_x.[19]

$$f_0 = (n \pm q_x)\, f_{\text{rev}} \qquad n \in \mathbb{N} \tag{2.37}$$

However, as the beam is not monochromatic and the chromaticity is unequal to zero, the present tune spread of the waiting beam requires the frequency to be modulated in order to excite all particles.
A general RF signal can be mathematically described with the following equation.[20]

$$A(t) = A_0 \cos\left(2\pi f_0 t + \phi(t)\right) \tag{2.38}$$

The resulting frequency of the signal can be derived with 2.39.

$$f(t) = f_0 + \frac{1}{2\pi}\frac{d\phi(t)}{dt} = f_0 + G(t) \tag{2.39}$$

$G(t)$ has to be chosen in such a way that the overall frequency matches all the frequencies present in the beam. Usually, a sawtooth-function is used as frequency modulating function $G(t)$ to cover the tune spread of the beam.[12][21]
Alternatively, also a noise signal can be used to modulate the frequency accordingly, as noise is composed of all different frequencies. This is the easiest function to implement in a simulation code, as it does not require a explicit time variable. For this reason, noise was used for the simulations of this thesis. However, it has to be stated that RF KO by noise is currently not used in accelerators for medical treatment.[22][23][24][25][26]
Additionally to the frequency modulation, also the kick amplitude A_0 has to be increased over the spill duration to achieve a constant extracted intensity.[20][24]

For RF KO, the parameter have to be chosen differently to the betatron core extraction.

1. A small momentum spread of the beam is favourable. As the momentum is not changed during extraction, the initial momentum distribution also defines both momentum offset and spread of the extracted spill.

2. The chromaticity should be set very low to reduce the effect of synchrotron motion of the beam during extraction. On the other hand, the chromaticity should be set to a (higher) value to fulfil the Hardt condition 2.34 for a high extraction efficiency. However, recent studies showed that the chromaticity with the highest extraction efficiency can deviate from the value defined by the Hardt condition.[27]

3. Preparatory simulations

Before the simulation of RF KO is performed, some preparatory simulations are done to get a better understanding for the extraction process. The results of these simulations are presented in this chapter.

3.1. Construction of the Steinbach diagram

The Steinbach diagram introduced in section 2.2.3 is an idealized theoretical description of the extraction process in amplitude-momentum space. To study the impact of lattice parameters on the extraction 'in reality' without any idealization, a simulation is performed to re-construct the Steinbach diagram.
For this, a grid of the size 100x100 is applied on the momentum-amplitude space[1]. Each grid point defines one particle, which results in a initial particle distribution of 10^4 particles. The particles are tracked for 1000 turns with default parameter settings ($Q_H = 1.6666$, $Q'_H = -4$, MXRk2 = 8.65). The simulation is static, which means that all parameter are constant during the whole simulation and no additional kicks are applied. The particle losses are recorded and mapped to the initial particle distribution to determine which particle with given initial amplitude and momentum is extracted at which turn. The in such manner re-built Steinbach diagram is shown in Figure 3.1.
The colour represents the turn number, at which the particle is extracted. The dark green region therefore marks the stable area, where the particles are not extracted at all. A dark red colour means that the particle is extracted very early (in the first few turns), while a yellow or light green colour stands for a later extraction.
The simulated Steinbach diagram shows that the linear approximation is only valid for a small momentum offset below roughly $\left|\frac{\Delta p}{p}\right| = 1 \cdot 10^{-3}$.
For high momentum offsets below $\frac{\Delta p}{p} = -7 \cdot 10^{-3}$, the stable amplitude decreases again. Further studies show that this is due to hitting another resonance, which enhances the instability of the particle motion. The corresponding horizontal tune was calculated as $Q_H = 1.75$, which pertains to the fourth-order resonance $4 \cdot Q_H = 7$.

[1] For simplification, the horizontal angle $x'_{\text{init.}}$ is set to zero for all particles, which means that the amplitude is equivalent to the horizontal position $x_{\text{init.}}$.

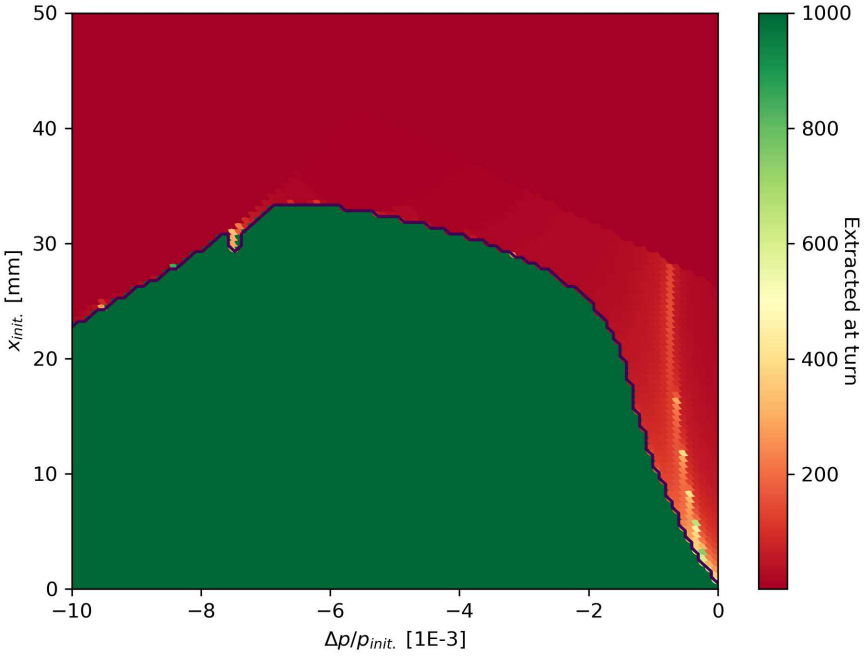

Figure 3.1.: Simulated Steinbach diagram for 10^4 particles and 1000 turns

Another observation from Figure 3.1 is worth mentioning. Intuitively, one would expect that the closer a particle is located to the stable area, the longer it takes until it is extracted. That would mean that the colour should change continuously from red over yellow to light green the closer one gets to the edge of the stable area. However, this is obviously not the case. Even just next to the Steinbach edge, the particles get extracted in less than 200 turns.

Additionally, a sharp curve appearing in light green and yellow is visible in the middle of the unstable area at low momentum offsets. Particles located on this curve are extracted significantly later than the their left or right neighbour particles with just slightly different momentum. This curve is present for all parameter settings and disappears when negative (instead of positive) initial particle positions are used.
The reason for the existence of this 'metastable curve' is the shape of the separatrix in phase space. As only the particle position is scanned while the angle is kept at zero, an iso-angular slice of the stable triangle is observed. According to Figure 2.6, going to positive positions at $X' = 0$ means to approach the fixed point P_1 and thus the branches of the separatrix. When the Kobayashi-Hamiltonian 2.30 is expanded to higher orders, small islands of stability appear near the branches of the separatrix in a fractal shape.

If a particle hits one of these islands, the resonant jumping of the particle pauses until the stable island is left again. This process is visible as delay in extraction and therefore as 'metastable curve' in the Steinbach diagram. The islands are only present at positive positions, which explains why the curve disappears when the particle position is switched to negative values.

3.1.1. Chromaticity correction

When the edge of the Steinbach diagram 3.1 is compared with the theoretical equation 2.35, a big discrepancy between the theoretical slope and the simulation results emerges, as the simulated slope in the linear region below $\left|\frac{\Delta p}{p}\right| = 1 \cdot 10^{-3}$ is steeper than it should theoretically be. This deviance is visualized in Figure 3.2, where the simulated (blue) and the theoretical (red) Steinbach diagram are superimposed.[2]

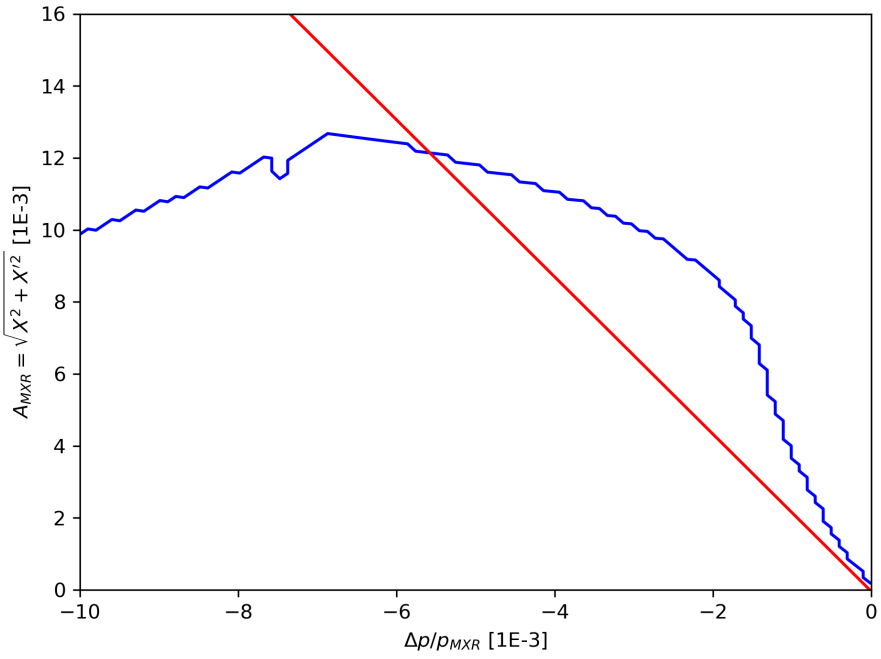

Figure 3.2.: Simulated (*blue*) and theoretical (*red*) Steinbach diagram at the resonant sextupole

[2]The simulated Steinbach diagram looks a little bit different to the one shown in Figure 3.1, as the particle amplitude is calculated at the position of the resonant sextupole instead of the starting point of the simulation to enable a comparison with the theoretical diagram.

According to equation 2.35, the chromaticity Q'_H, the momentum offset $\frac{\Delta p}{p}$ and the strength of the resonant sextupole S affect the Steinbach diagram. As it was confirmed in the output files of the simulation that the external parameter momentum offset and MXR strength are set correctly, the source of the difference has to be the chromaticity. Although the chromaticity listed in the TWISS output file shows the correct value, off-momentum particles seem to 'feel' a different chromaticity during the tracking than the one set.

To confirm this hypothesis, the real chromaticity that affects the off-momentum particles has to be calculated. This can be done via a Fourier analysis of the particle position in dependence of the turn number. As the tune is the number of particle oscillations per turn, it can be thought of as a 'oscillation frequency' if the time unit is one turn. Thus, the peak of the Fourier transform of the horizontal particle position corresponds to the tune that affects the particle.[3] The chromaticity can be obtained by dividing the difference between set on-momentum tune and the calculated 'real' off-momentum tune by the momentum offset of the particle.
The Fourier analysis was performed for different tune and chromaticity settings and a momentum offset of $\frac{\Delta p}{p} = -0.2\%$ to investigate the impact of the chosen setpoint on the chromaticity error. The results are visualized in Figure 3.3.

It can be seen that the set chromaticity strongly influences the resulting relative chromaticity error. While the error is between 20 and 30% for $Q'_H < -5$, the 'real' chromaticity is wrong by more than 100% for a low absolute chromaticity values. This means that when a value of $Q'_H = -1$ is set via MAD-X, a particle with an off-momentum of -0.2% 'feels' a doubled chromaticity of $Q'_H = -2$.
Another observation is that the set tune value does not influence the relative chromaticity error strongly, as the contour lines are almost vertical. However, a slight trend that a tune setpoint close to resonance increases the relative chromaticity error can be noticed.

[3] More specific, the position of the peak of the Fourier transform denotes the difference of the tune to the closest next integer. As the next integer for the tunes used for extraction is 2, the peak position of the Fourier analysis has to be subtracted from 2 to obtain the tune value.

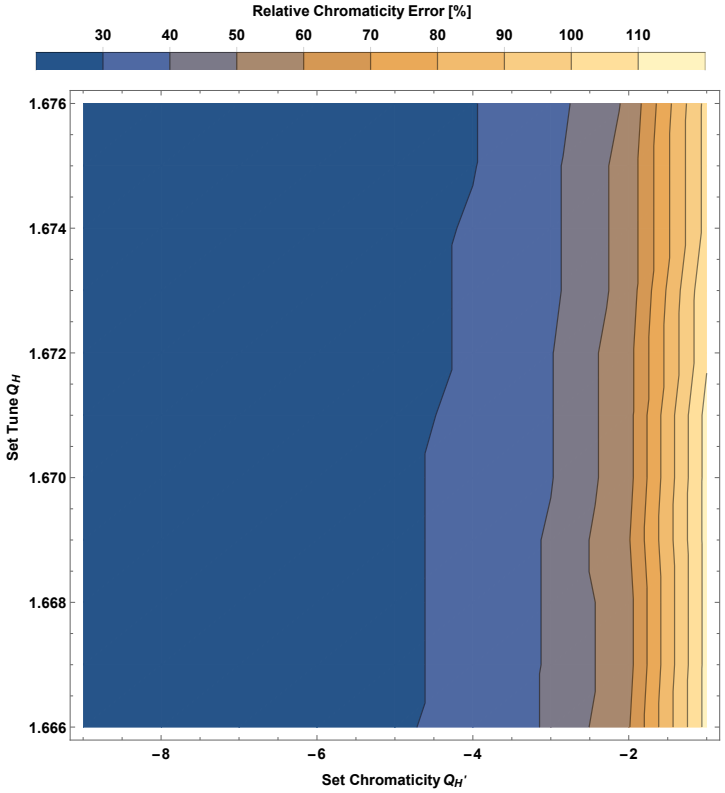

Figure 3.3.: Relative chromaticity error for different tune and chromaticity settings

With the knowledge that the chromaticity is different to the one set, the construction of the Steinbach diagram has to be further analysed. For this, the simulation was repeated, but this time the chromaticity was calculated for all particles via Fourier analysis as described above. The results are shown in Figure 3.4.

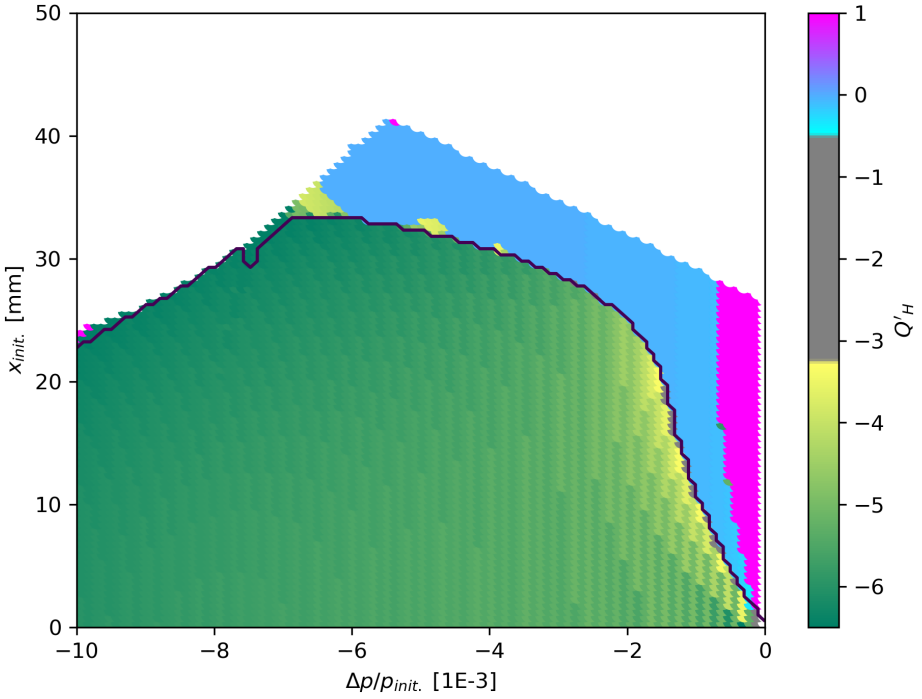

Figure 3.4.: Steinbach diagram with calculated chromaticity values

The first observation is that all particles outside the stable region of the Steinbach diagram 'feel' a chromaticity of zero. This is not surprising, as these particles are resonant and are therefore all affected by the resonant tune $Q_H = 1.666$, independent of their momentum.
The pink area right of the metastabile curve originates from the low momentum offset in this region, which leads to high chromaticity values when the division is carried out.
It is also visible that there is a momentum dependency of the real chromaticity of the stable particles. Particles with a small momentum offset tend to be closer to (or even below) the set chromaticity of -4. The greater the momentum offset is, the bigger is the chromaticity deviation. The overall chromaticity change is between 30 and 50%, as expected from Figure 3.3.

This chromaticity shift has to be taken into account for all future simulations, especially when calculations with the chromaticity value are performed.

3.1.2. Parameter scans

As second part of the analysis, it is investigated how the Steinbach diagram changes under parameter modification.
Either the tune, the chromaticity or the strength of the resonant sextupole is changed, while the other two parameter are fixed at their respective default value. A initial particle grid of 10^4 particles is created as described in the previous section and tracked for 1000 turns while recording the turn number at which the particle is lost. Contrary to the last section, also positive momentum offsets are allowed by setting the extreme momentum values for the initial grid to $\frac{\Delta p}{p} = \pm 10 \cdot 10^{-3}$.
For each parameter scan, three exemplary Steinbach diagrams are shown to visualize how its shape changes.

Tune scan

When the tune is changed, the resonance moves to a different offset momentum. As the chromaticity $Q'_H = -4$, a tune change of one unit moves the resonance by $\frac{1}{4}$ units.
This expected reaction is confirmed by the simulation, as shown in Figure 3.5. The valley of the stable region moves to the right by approximately the calculated distance. As the aperture line is invariant under any lattice parameter changes and, moreover, the fourth-order resonance valley is moved into the observed momentum parameter space by increasing the tune, also the shape of the stable area is affected. However, the slope of the Steinbach edge and the metastable curve remain the same for all tune values.

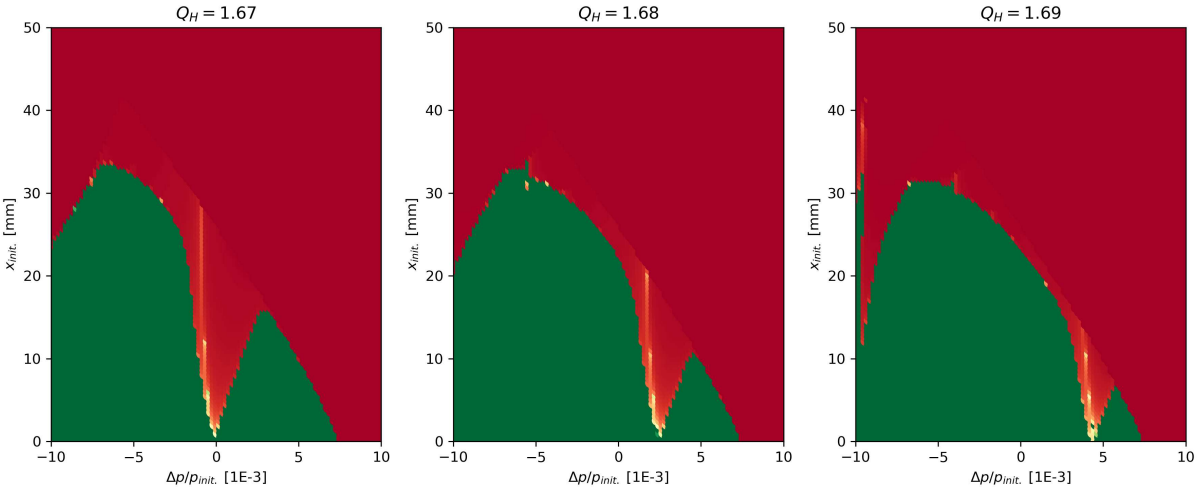

Figure 3.5.: Steinbach diagram for different tunes

Chromaticity scan

According to equation 2.35, the slope of the Steinbach diagram is directly proportional to the absolute value of the chromaticity. A lower absolute value of Q' leads to a flatter Steinbach curve. This expected behaviour is verified by the results of the simulation, which is plotted exemplary for three different chromaticity values in Figure 3.6.

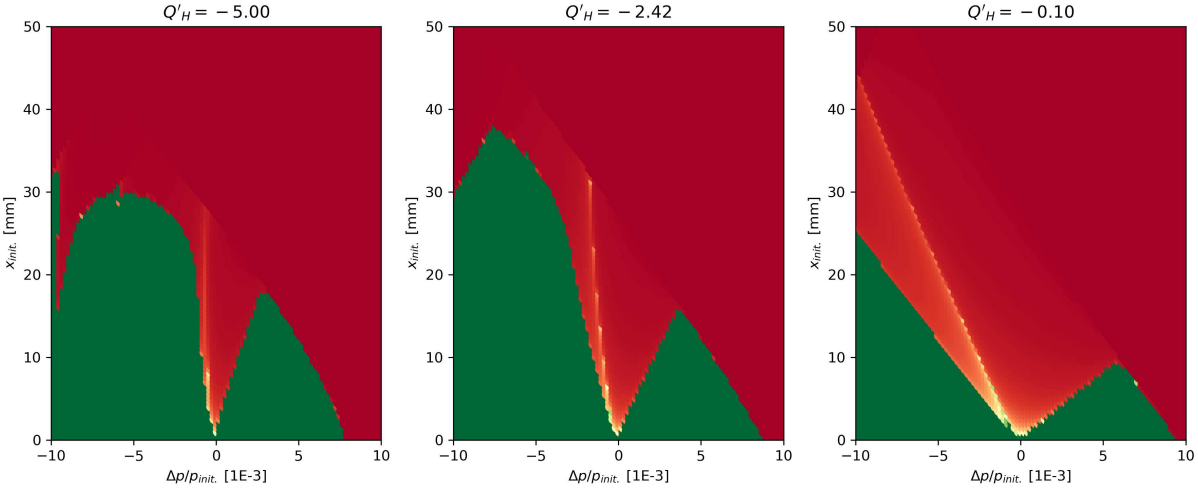

Figure 3.6.: Steinbach diagram for different chromaticities

MXR strength scan

Equation 2.35 also predicts an inverse proportionality of the slope of the Steinbach edge with respect to the strength of the resonant sextupole S. Likewise, the simulation confirms this expectation as the slope increases as the sextupole gets weaker. The Steinbach diagrams for three different sextupole strengths are shown in Figure 3.7.

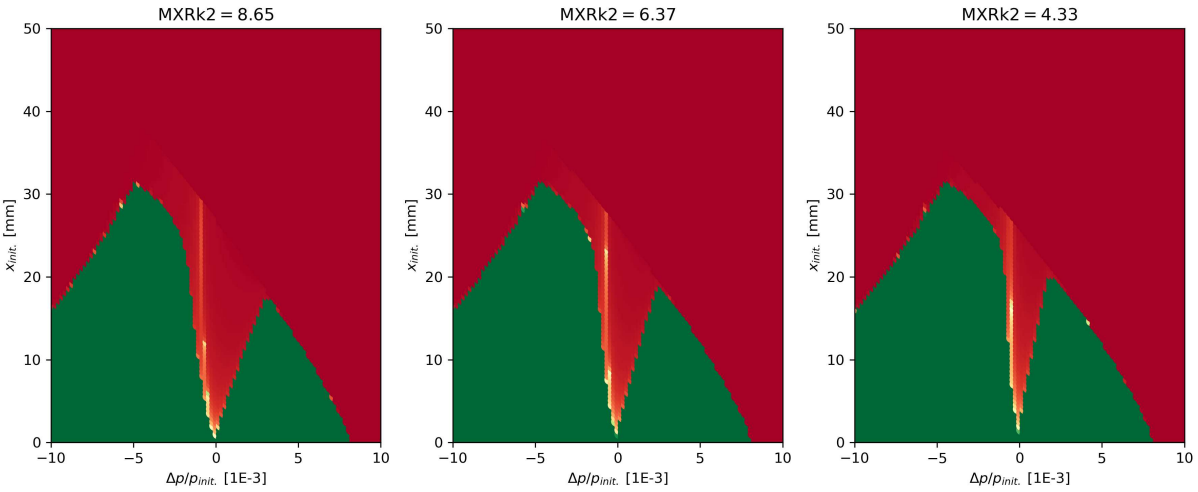

Figure 3.7.: Steinbach diagram for different strengths of the resonant sextupole

3.2. Simulation of betatron core extraction

To define a benchmark as well as a base for comparing RF KO to, the betatron core driven extraction was simulated via MAD-X. The structure of the MAD-X script used for all simulations of this thesis can be found in Appendix A.
The betatron core was introduced as an arbitrary matrix element, which increases the momentum of the particles by applying a constant kick in longitudinal direction.[4]
To estimate the kick strength of the betatron core, it has to be taken into account that the spill has a momentum spread of $\frac{\Delta p}{p} = 4 \cdot 10^{-3}$ after phase jump. To save computation time, the simulation of the whole extraction process is designed to be finished within 10^5 turns. Therefore, the betatron core has to apply a longitudinal kick with a strength of $4 \cdot 10^{-8}$ every turn. For practical reasons, a value of $5 \cdot 10^{-8}$ was set as betatron core strength for the simulation.

3.2.1. Creating the initial particle distribution

The initial particle distribution with 1000 particles was created via Python. A Gaussian distribution is used for the horizontal position x and the horizontal angle x', while the momentum $\frac{\Delta p}{p}$ is uniformly distributed around the central offset value of $-3.5 \cdot 10^{-3}$ with a total spread of $4 \cdot 10^{-3}$.
A RMS geometrical horizontal emittance of $1.4286\,\pi$ mm mrad was used according to the Main Ring design report [6][28]. The standard deviation for x and px can be calculated from the emittance with the equations 3.1, where β_x denotes the value of the horizontal beta function at the position where the tracking is started.[5]

$$\begin{aligned} \sigma_x &= \sqrt{\epsilon_x * \beta_x} \\ \sigma_{px} &= \sqrt{\frac{\epsilon_x}{\beta_x}} \end{aligned} \tag{3.1}$$

For the vertical plane, the position y and the angle y' are set to zero for all particles of the distribution, as the whole extraction process takes place in the horizontal plane and therefore it is expected that the vertical phase space does not influence the extraction. It was confirmed later by a simulation with a Gaussian distribution also in vertical plane that this assumption is valid.

[4] A longitudinal kick affects the particle momentum, which is the sixth coordinate in 6D phase space. Therefore, the MAD-X command *KICK6* has to be used.
[5] Equations 3.1 are only valid because the horizontal alpha function α_x is zero at the start of the tracking.

The parameter used to create the initial particle distribution is summarized in Table 3.1.[28][29][30][31]

Table 3.1.: Parameter of the initial particle distribution for betatron core simulation

Parameter	**Value**
RMS geom. emittance ϵ_x	$1.4286\,\pi$ mm mrad
position standard deviation σ_x	3.513 mm
angle standard deviation σ_{px}	0.361 mrad
central momentum offset $\left(\frac{\Delta p}{p}\right)_{\text{center}}$	$-3.5 \cdot 10^{-3}$
total momentum spread $\left(\frac{\Delta p}{p}\right)_{\text{spread}}$	$4 \cdot 10^{-3}$
maximum momentum $\left(\frac{\Delta p}{p}\right)_{\text{max}}$	$-1.5 \cdot 10^{-3}$
minimum momentum $\left(\frac{\Delta p}{p}\right)_{\text{min}}$	$-5.5 \cdot 10^{-3}$

The initial particle distribution is also plotted and further analysed, as shown in Figure 3.8. The real horizontal phase space as well as the normalized phase space are plotted. Additionally, a histogram of x, x' and $\frac{\Delta p}{p}$ is drawn. A fitting of the histogram for position and angle with a Gaussian function yields to a mean value of close to zero and a standard deviation consistent with the values in Table 3.1.

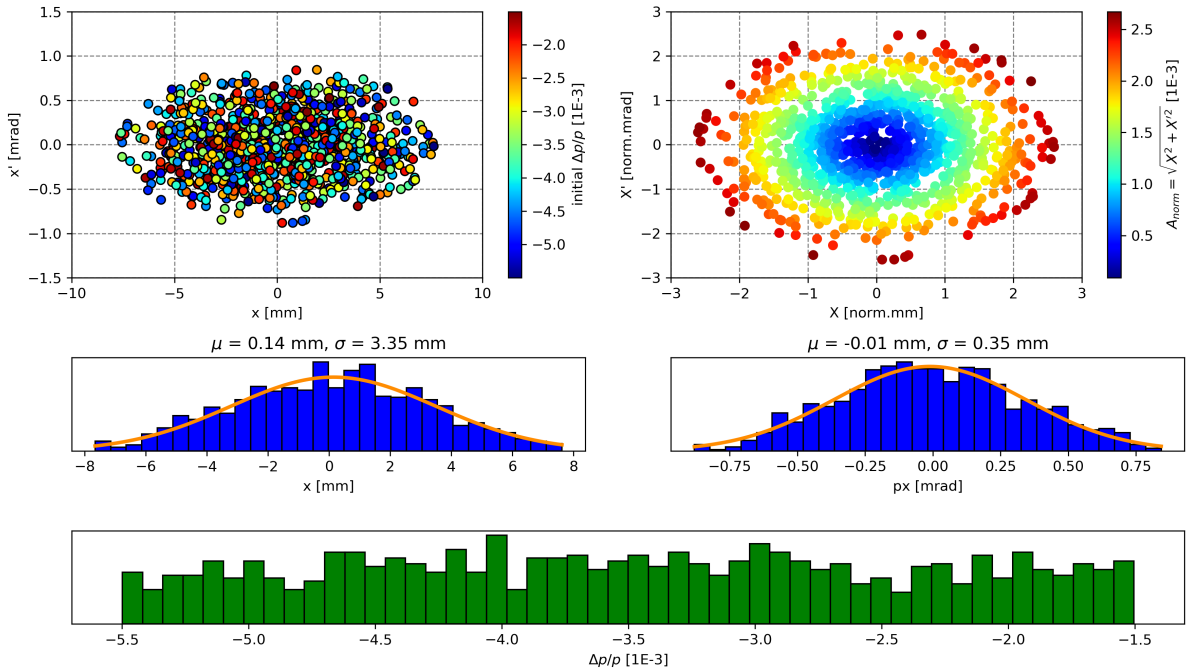

Figure 3.8.: Initial distribution for betatron core simulation.
Top left: Real horizontal phase space, color-coded particle momentum
Top right: Normalized horizontal phase space, color-coded normalized particle amplitude
Center left: Histogram of the initial horizontal position distribution
Center right: Histogram of the initial horizontal angle distribution
Bottom: Histogram of the initial particle momentum distribution

3.2.2. Results of the simulation

The results of the simulation of the betatron core extraction are shown in Figure 3.9. From the initially 10^3 particles, 97% were extracted at the ESE. The remaining 3% were lost somewhere else in the Main Ring during the process.

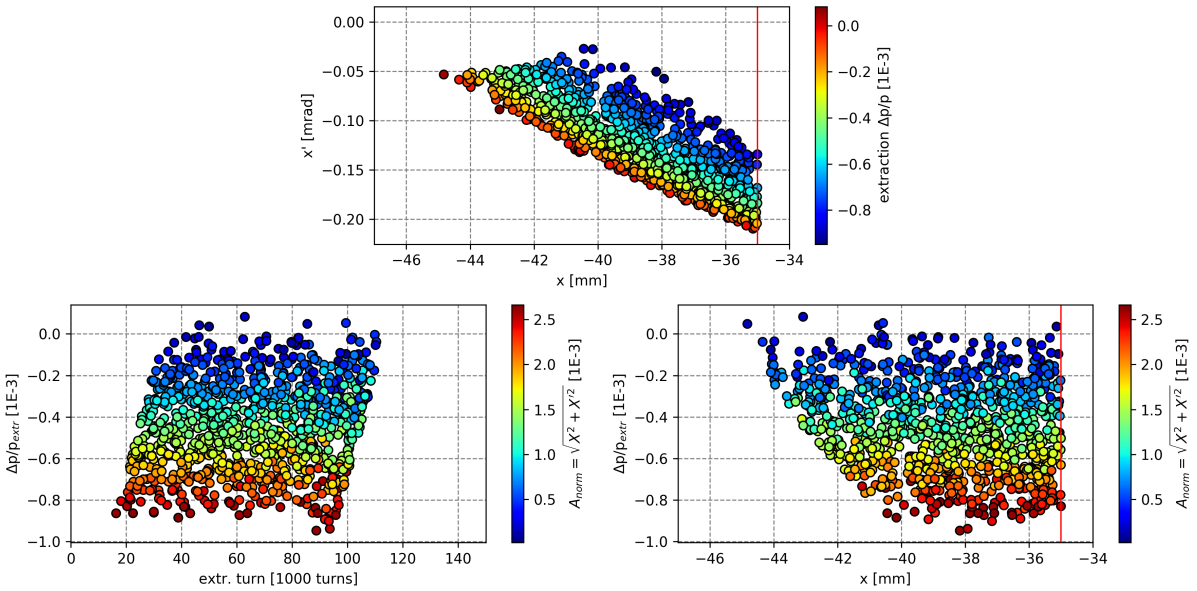

Figure 3.9.: Results of the betatron core simulation
Top: Phase space of the extracted particles at the ESE, color-coded particle momentum
Bottom left: Particle momentum vs. extraction turn number, color-coded normalized particle amplitude
Bottom right: Particle momentum vs. position at extraction, color-coded normalized particle amplitude

The plot at the top shows the phase space at the electrostatic septum for the extracted particles. The wire of the ESE at $x = -35\,\text{mm}$ is marked with a vertical red line. The low-momentum particles (marked in blue) are located on the top of the distribution, which means that they are extracted with a higher average angle and position. The red high momentum particles are extracted with lower average angles and positions and are therefore on the bottom of the distribution.
The shape of the distribution of the extracted particles can be explained with the phase space of the particles during extraction, which is shown later in Figure 3.10.
At the bottom left, the momentum of the extracted particle is plotted over the extraction

turn number. Two interesting features can be seen: Firstly, it is clear that the particles with a higher amplitude are extracted earlier than the ones with a small amplitude. Secondly, a higher particle amplitude is directly correlated to a lower extraction momentum. Both observations are perfectly consistent with the Steinbach diagram, when the movement of the stack into resonance by increasing the momentum is taken into account. Therefore, the tilted edges on the left and the right of the distribution are corresponding to the stopband of the Steinbach diagram.
The third plot at the bottom right shows the particle momentum over horizontal position of the extracted particle. One can observe that a higher momentum (and therefore a lower particle amplitude) corresponds to a bigger spiral step and vice versa. The spiral step varies from 10 mm for the on-momentum particles to 5 mm for the low-momentum particles with $\frac{\Delta p}{p} = -1 \cdot 10^{-3}$.

The phase space for the last 1000 turns before extraction is plotted in Figure 3.10. The third-order resonant extraction is visible at the triangular-shaped separatrix before a particle is extracted. Furthermore, it can be seen that the separatrices for all particles with different momenta overlap for the extraction 'branch', which results in a narrow angular distribution of the extracted particles. This overlapping is a consequence of the Hardt condition, which is fulfilled by design for the parameter for betatron core extraction.[6][16][32]

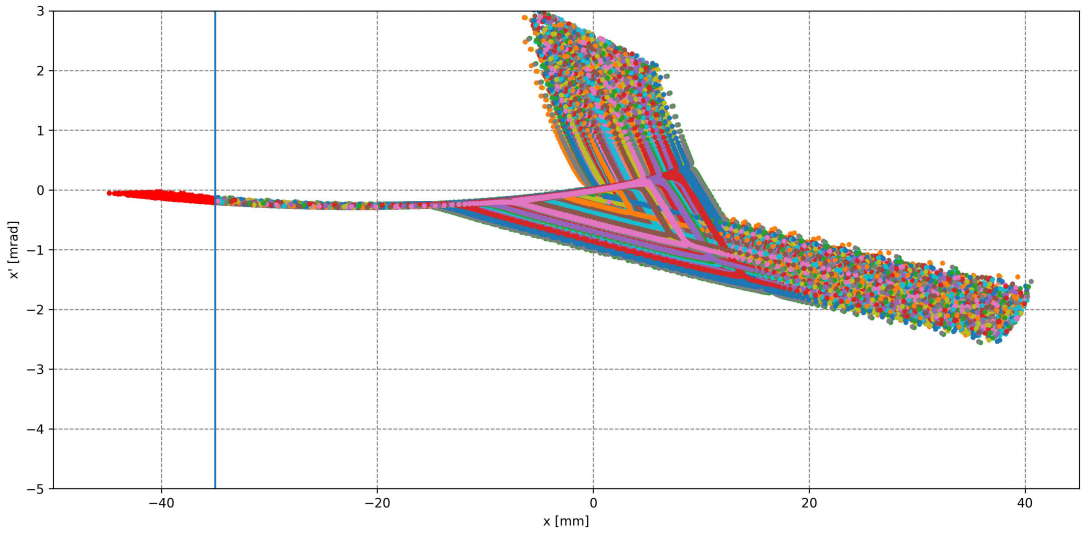

Figure 3.10.: Phase space at the ESE for the last 1000 turns before extraction.
Each color represents one particle, the ESE wire position is marked as vertical line and the extracted particles are shown in red.

4. Simulation of the Radio Frequency Knockout extraction

After simulating betatron core extraction as benchmark, the actual RF KO process is simulated. For this, the MAD-X structure created for betatron core extraction can be re-used, but some essential changes have to be implemented.
At first, the matrix element representing the betatron core has to be adapted so that it represents a transverse kicker and can be used as knockout exciter (KOE). As the extraction driven by RF KO takes place in horizontal plane, the kicker has to give a kick in horizontal direction, i.e. influencing the angle x' of the particles.[1]
The position of the kicker in the Main Ring lattice is not changed, it is therefore installed at the position of the betatron core. This cannot be realized in reality, as the kicker used for RF KO would have to be installed at a different location due to space limitations. However, it was confirmed in a later simulation that the position of the KOE does not affect the extraction process qualitatively.

As a second important change, the kick strength of the KOE must not be the same every turn. A constant transverse kick would decrease the particle amplitude every three turns due to the third-order resonance, which destroys the underlying principle of RF KO. Because of this, the kick strength has to be different from turn to turn.
Additionally, as mentioned earlier, the whole tune/momentum spread of the beam has to be excited. For the first simulation, this is realized using noise as excitation pattern. A macro changes the kick strength of the kicker every turn according to equation 4.1.

$$k_{\text{noise}} = A_{\text{noise}} \cdot \text{random}(0, 1) \tag{4.1}$$

A_{noise} is the amplitude of the noise, which is set to $5 \cdot 10^{-5}$ for the first simulations, but can be modified later to change the speed of extraction. The random function in 4.1 produces a uniformly distributed random number between 0 and 1. Thus, the kick strength is re-evaluated every turn and is randomly assigned with a value between 0 and A_{noise}.

[1] In terms of programming, the *KICK6* command used for betatron core extraction has to be changed to a *KICK2* command for RF KO.

Thirdly, also the initial particle distribution has to be modified for RF KO. Different to betatron core extraction, the waiting stack is not moved horizontally into resonance by increasing the particle momentum, but the particle amplitude is increased until it reaches the edge of the Steinbach diagram. Therefore, the momentum spread can be reduced to decrease the sensitivity for ripples. A momentum spread of $\left(\frac{\Delta p}{p}\right)_{\text{spread}} = 5 \cdot 10^{-4}$ is used for the simulation, which is almost a factor 10 smaller than the spread for betatron core extraction.

The goal of the simulation is to find a set of parameter, for which the extraction process fulfils the following requirements:

- The phase space of the extracted particles at the ESE should be as similar as possible to the one for betatron core extraction. If position, angle and momentum of all particles at the electrostatic septum are almost identical for both extraction processes, the trajectory of the particles after the ESE to the magnetostatic septum and further via the transfer line to the treatment rooms is also similar for both cases. Therefore, the steering process of the transfer lines can be done similar to the already commissioned betatron core extraction and no big differences are expected, which minimizes the needed additional effort.
- The extraction efficiency should be reasonably high. This requirement ensures that the particle losses before and during extraction are small.
- The extraction should be insensitive to small changes of the tune, the chromaticity and the strength of the resonant sextupole. The working point should be located at a plateau with respect to the mentioned parameter.
- The spiral step should be close to 10 mm.

To fulfill these requirements, a multi-dimensional optimization was performed by varying the following parameter:

- Horizontal tune Q_H
- Horizontal chromaticity Q'_H
- Strength of the resonant sextupole MXRk2
- Central momentum offset of the initial particles $\left(\frac{\Delta p}{p}\right)_{\text{center}}$

Although the ultimate goal of RF KO implementation is a bunched beam extraction, the simulations for this thesis do not contain a cavity element, as it focuses purely on transverse simulation. The longitudinal beam behaviour as well as its effect on the transverse dynamics and on intensity ripples is out of the scope of this thesis.

4.1. The extraction diagram

To visualize the extraction efficiency in dependence of a certain parameter and to analyze the reason for possible particle losses, a so-called *extraction diagram* is used, as exemplary shown in Figure 4.1.

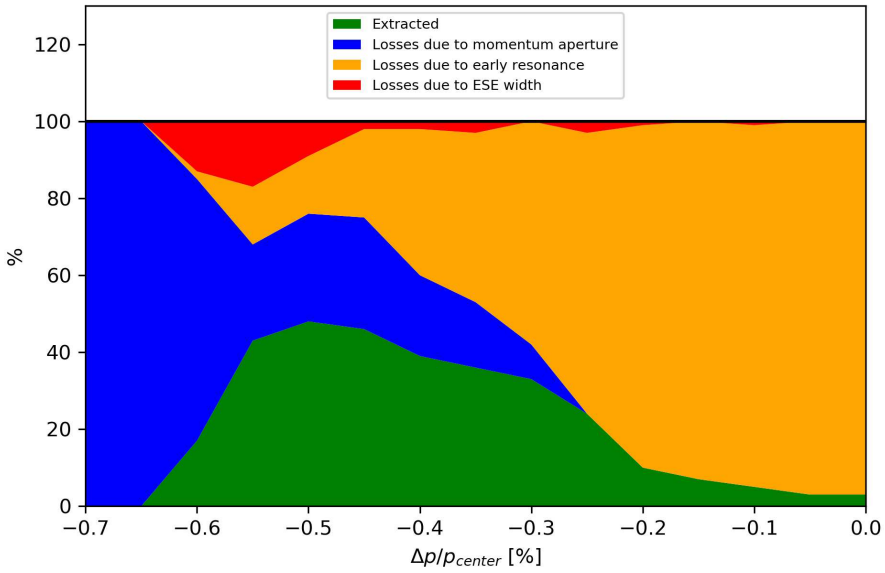

Figure 4.1.: Example of an extraction diagram

An extraction diagram is a stack plot of four different curves in dependence of a parameter, which is in case of Figure 4.1 the central momentum offset. Each colour represents a different curve and thus a different reason that a particle is removed from the distribution in the Main Ring.

- The green area represents the fraction of the particles that get extracted properly at the ESE, which means that the extraction efficiency can be directly read from this curve.
- The blue area visualizes the percentage of the particles that get lost anywhere else but the ESE. These losses occur when a particle exceeds the aperture of any element in the Main Ring lattice, which happens if an off-momentum beam is lost in high-dispersive regions. An enlarged blue area means that the particles are too far away from resonance.
- On the other side, the yellow area denotes the particles that are extracted even before the kick of the KOE is turned on, i.e. during the ramping of the MXR or during the

'waiting time'. This means that the particle is too close to the resonance and the extraction happens too early.

- Finally, the red area represents particles with a too small spiral step. As an effective ESE width of 0.5 mm (instead of the design value of 0.1 mm for a conservative loss estimation) is used for the simulation, all particles with a spiral step smaller than this value are considered as lost. The value of the effective ESE width is a very conservative estimate, so the losses might be over-estimated.
  Losses due to the ESE width occur when a particle is too far away from resonance, but already hits the ESE wire without being resonant. In this case, the spiral step is close to zero, as the non-resonant particles do not jump from branch to branch of the separatrix while increasing the amplitude as they would in resonance.

As the four options mentioned above are the only possibilities how a particle can be lost or extracted during the extraction process, the curves add up to 100% for every parameter value. Because of this, a stack plot can be used to visualize the quality of the extraction process over a scanned parameter.
The parameter used as abscissa for an extraction plot can be chosen freely. However, as the goal of the simulation is an optimisation with respect to tune, chromaticity, momentum offset and strength of the resonant sextupole, it makes sense to use these optimisation variables also for the extraction diagram.

4.2. Proof of the Radio Frequency Knockout principle

To check the proper reproducibility of the RF KO mechanism with MAD-X, the simulation is set up as described above and one particle with $x = px = y = py = 0$ is tracked for 150000 turns with different momentum offsets. The design horizontal tune $Q_H = 1.666$ and the design nominal strength of the resonant sextupole (MXRk2 = 8.65) is kept, while the chromaticity is set to $Q'_H = -1$ to reduce the slope of the Steinbach diagram and thus the amplitude needed for extraction.
The results of the simulation for the proof of principle is shown in Figure 4.2.

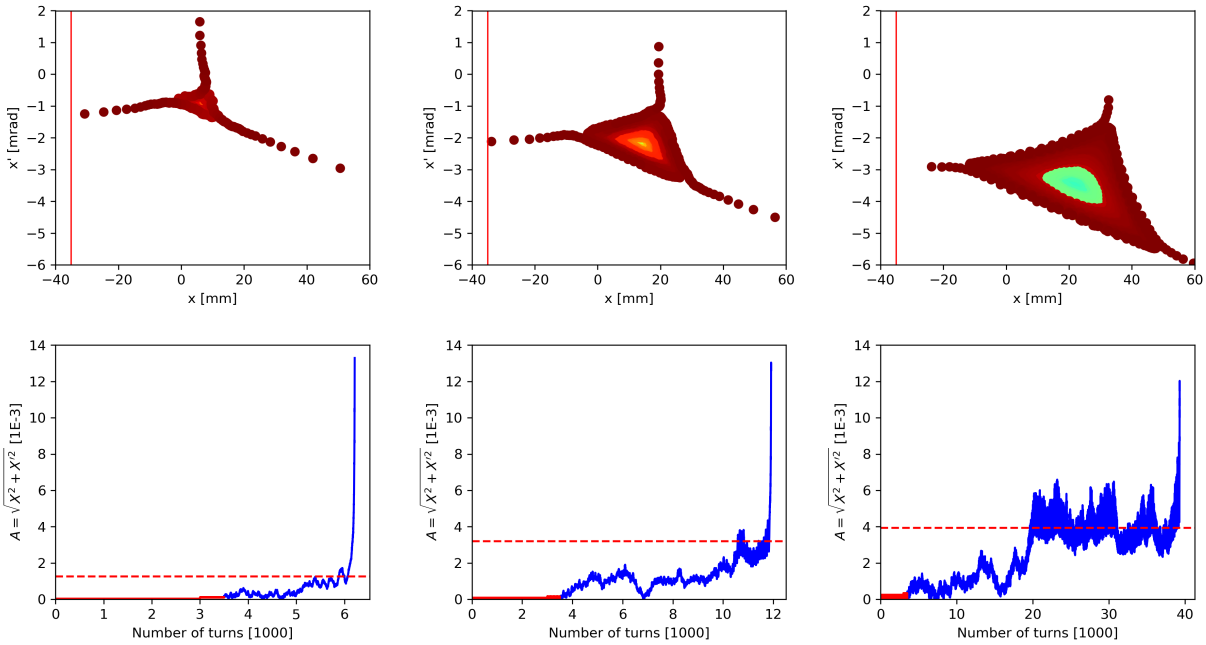

(a) $\frac{\Delta p}{p} = -1.5 \cdot 10^{-3}$ (b) $\frac{\Delta p}{p} = -3.5 \cdot 10^{-3}$ (c) $\frac{\Delta p}{p} = -5.5 \cdot 10^{-3}$

Figure 4.2.: Results of the proof of principle simulation of RF KO.
Phase space (top) and normalised dispersion-free amplitude vs. number of turns (bottom) for different momentum offsets.

The top row of Figure 4.2 shows the phase space of the particle before it is extracted. The area of the separatrix increases from left to right, i.e. when the momentum offset is more distant to zero. This is the expected behaviour as the stable triangle gets bigger with increasing distance to the resonance. The shifting of the separatrix to higher horizontal positions and lower angles with lower momenta can be explained with the dispersion, which

affects the particle coordinates according to equation 4.2.

$$\begin{pmatrix} \Delta x \\ \Delta x' \end{pmatrix} = \begin{pmatrix} D_x \\ D'_x \end{pmatrix}_{\text{ESE}} \cdot \frac{\Delta p}{p} \tag{4.2}$$

At the position of the ESE, $D_x \approx -4$ and $D'_x \approx 0.6$. Therefore, a more negative momentum offset shifts the particle in phase space to the bottom right, which is the trend observed from the simulation results.

The normalized amplitude is plotted over the number of turns in the bottom row of Figure 4.2. It is important to mention that the impact of the dispersion at the ESE on the amplitude was removed by subtracting the dispersive part with equation 4.3.

$$\begin{pmatrix} x \\ x' \end{pmatrix} \rightarrow \begin{pmatrix} x \\ x' \end{pmatrix} - \begin{pmatrix} D_x \\ D'_x \end{pmatrix}_{\text{ESE}} \cdot \frac{\Delta p}{p} \tag{4.3}$$

This adoption is necessary to extract the part of the amplitude that actually originates from the RF KO process. After the subtraction, the coordinates were also normalized to analyse the normalized phase space.
The KOE is turned on after 3500 turns, which is marked as transition from red to blue line in Figure 4.2. The horizontal dashed red line is the by equation 2.35 calculated limit for the amplitude before a particle gets unstable, which corresponds to the edge of the Steinbach diagram at a given momentum.[2]

The plots show that the extraction takes the longer the bigger the absolute value of the momentum offset is, which is again correlated to the distance to resonance.
The theoretical amplitude limit fits quite well the point where the particle gets unstable. However, the calculated limit seems to be slightly too low, especially for the highest momentum offset. This can be explained by taking into account that equation 2.35 is only valid in a linear regime, where all effects of higher order can be neglected. The more distant a particle is from resonance (i.e. the higher the absolute value of the momentum offset is), the more important effects of higher order get, which explains the discrepancy between calculated and simulated amplitude limit as well as the deviance of the simulated Steinbach diagram 3.1 from the theoretically expected linear behaviour, especially for particles far away from resonance.
Another explanation for the deviation is the randomness of the kick. A particle which just exceeded the stable amplitude limit can be kicked back by a suitable kick strength and become stable again. This re-stabilization also leads to a under-estimation of the actual amplitude limit.

[2] As explained in 3.1.1, the set chromaticity value cannot be used for the calculation. Q'_x has to be obtained from a Fourier analysis.

4.3. Scenarios for Radio Frequency Knockout

To avoid that particles are on resonance while ramping the sextupole and get extracted immediately in an uncontrolled way, the waiting beam has to be moved away from the resonant tune. This can be done by either changing the tune ('off-tune') or the central momentum of the particles ('off-momentum'), as a momentum offset is equivalent to a tune offset by equation 4.4.

$$\Delta Q = Q' \cdot \frac{\Delta p}{p} \tag{4.4}$$

During simulation, it was found out that also the situation of a tune offset and an additional momentum offset has to be taken into account to find the scenario that fits best the prerequisites. The reasons for the need of this third scenario is discussed later.

Overall, three different scenarios have to be investigated separately:

- On-tune and off-momentum
- Off-tune and on-momentum
- Off-tune and off-momentum ('Hybrid' scenario)

Each scenario is analysed and a parameter optimization is performed to find the most promising candidate for RF KO. The simulations are evaluated by creating extraction diagrams with Python to investigate how a parameter variation affects the extraction process.

4.3.1. On-tune, off-momentum scenario

For this scenario, the tune is fixed at resonance $Q_H = 1.666$ and the chromaticity, the strength of the resonant sextupole and, most importantly, the momentum offset can be varied. The extraction diagram for a scan of the momentum offset from -0.5% to 0 is plotted in Figure 4.3 for different MXR strengths.

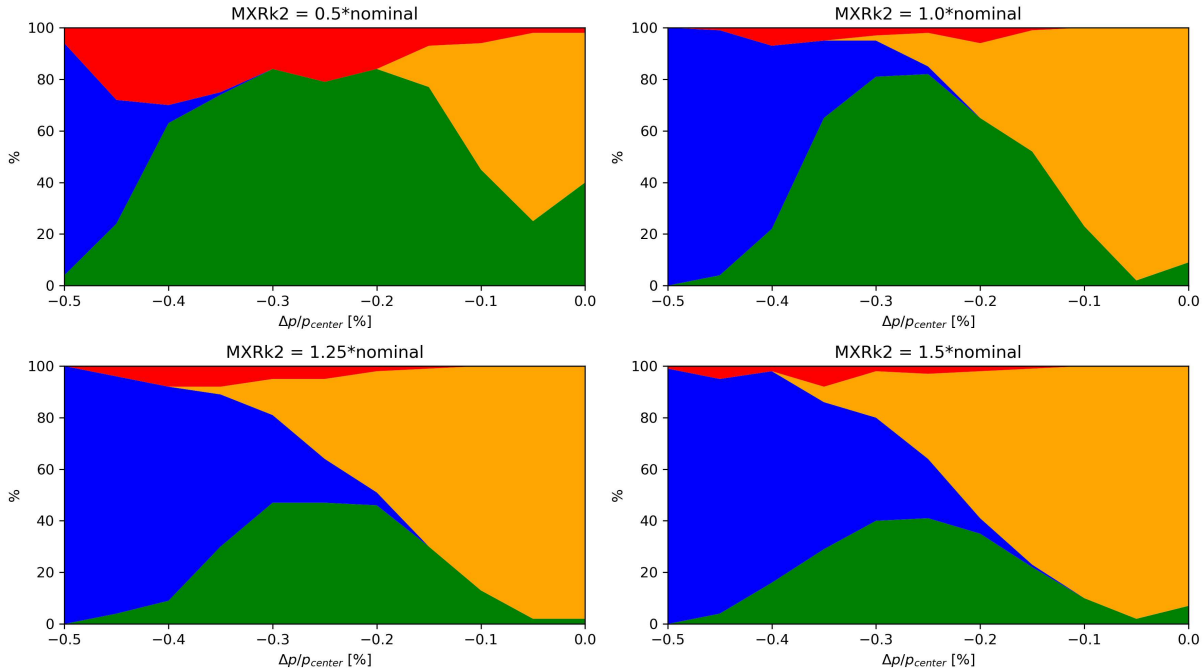

Figure 4.3.: Extraction diagram for a scan of the momentum offset at different MXR strengths for the on-tune, off-momentum scenario

The simulations show the reasons for particle losses at different momentum offsets. Low central momentum offsets correspond to a proximity to the resonance, which leads to losses due to early resonance (yellow). For higher offsets, dispersion leads to losses of the particles due to the aperture of the lattice elements (blue). The effective ESE width causes very few losses, as the red area is very small. Its impact is the highest for the lowest sextupole strength, as the spiral step is proportional to S.

Overall, the simulation shows that the on-tune, off-momentum scenario is not a suitable solution to meet the requirements defined above. For high sextupole strengths in the bottom row of Figure 4.3, the extraction efficiency is unacceptably low at below 50%. For lower strengths (top row), the extraction efficiency at least reaches 80%. However, the losses caused by dispersion inhibit the formation of a stable plateau, which can be easily improved by moving the tune instead of the momentum offset. For the lowest sextupole strength, the phase space shows that the spiral step gets to small, which also leads to increased losses due to the non-zero width of the septum.
Due to the mentioned objections, it was decided to reject the on-tune, off-momentum scenario and to focus on the other two schemes.

4.3.2. Off-tune, on-momentum scenario

In contrast to the first scenario, the momentum offset is here fixed at $\frac{\Delta p}{p} = 0$, which means that the tune is altered in order to control extraction.
Analogously to the on-tune, off-momentum scenario, the extraction efficiency is simulated for different strengths of the resonant sextupole. However, the scanned parameter is the horizontal tune Q_H instead of the momentum offset, which is fixed at zero. The extraction diagrams for a tune scan from resonant tune $Q_H = 1.6666$ to 1.676 is shown in Figure 4.4. Important considerations regarding this scenario are provided in the next section.

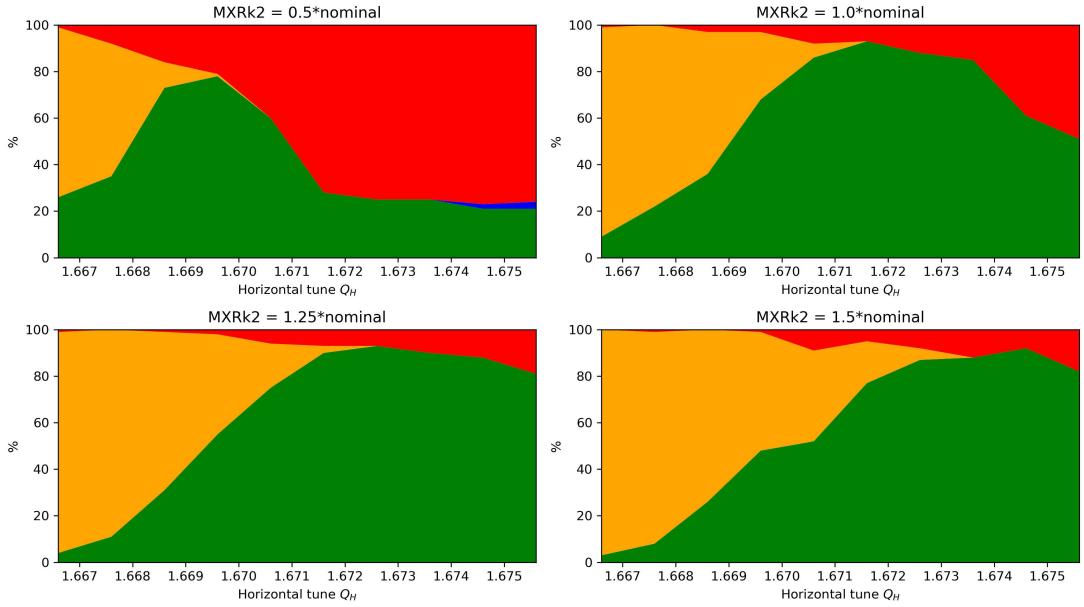

Figure 4.4.: Extraction diagram for a tune scan at different MXR strengths for the off-tune, on-momentum scenario

As expected, the losses due to dispersive effects (blue area of the extraction diagram) are almost vanished, as the momentum offset is zero. In comparison with Figure 4.3, the yellow area moved from right to left, as the abscissa is changed from momentum offset to tune at negative chromaticity.
A stronger resonant sextupole increases the size of the spiral step, which corresponds to a reduction of the losses due to the non-zero width of the electrostatic septum (red area). As the ESE width losses are predominant at higher tunes (which can be explained considering that for high tunes, the particle are farther away from resonance and therefore the spiral step is not big enough yet when hitting the ESE wire), the maximum of the extraction

efficiency is shifted to higher tunes for larger strengths of the resonant sextupole.
To analyse the impact of the chromaticity on the extraction efficiency, the simulation was repeated for different values of Q'_H at a 125% of the nominal resonant sextupole strength. The extraction diagrams of these simulations are shown in Figure 4.5. The design chromaticity for the MedAustron lattice was chosen to fulfil the Hardt condition 2.34 and is calculated as $Q'_H = -4.041$.[6]

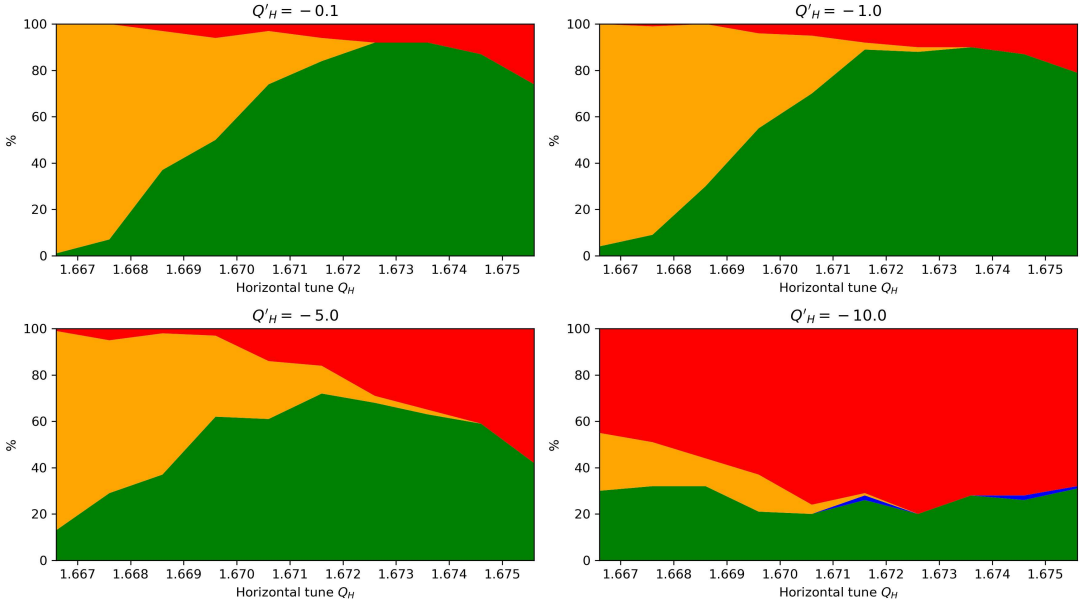

Figure 4.5.: Extraction diagram for a tune scan at different chromaticity values for the off-tune, on-momentum scenario

As the chromaticity converts the momentum variance $\frac{\Delta p}{p}$ to tune difference ΔQ, the tune spread for a constant momentum spread increases with higher absolute chromaticity values. This varying tune spread causes two effects:

1. For tune values close to resonance, high chromaticity leads to an increased tune spread. Thus, the particles with non-zero momentum are moved further away from resonance and therefore the losses due to hitting resonance too early are reduced. This is visible as reduction of the yellow area for higher chromaticity values.

2. For tunes that are already far away from resonance, a high chromaticity means that off-momentum particles are even more distant to $Q_H = 1.6666$. Because of this, the red area representing particles that hit the ESE before being resonant increases for higher absolute chromaticity values.

4.3.3. Hybrid scenario

Figure 4.5 shows a promising extraction efficiency for $Q'_H = -1$, but there is still a big region near resonance which is dominated by losses due to early extraction, as these particles are too close to resonance. These early extractions avoid the formation of a plateau with high extraction efficiency.
This limitation can be overcome by two approaches. The first possibility would be to move to even higher tunes to be more distant to resonance. However, this would mean that effects of higher order have to be taken into account, what would complicate the whole extraction process. Additionally, if the tune is too far away from resonance, the particles might hit the ESE without being resonant and therefore the extraction efficiency would be reduced.
The second option is to keep the tune where it is, but to add an additional momentum offset to all particles. This means that the extraction is both off-tune and off-momentum. To confirm that the addition of a momentum offset improves the situation, simulations were performed for different momentum offsets. The results for momentum offsets of -0.2%, 0% and $+0.2\%$ are presented in Figure 4.6.

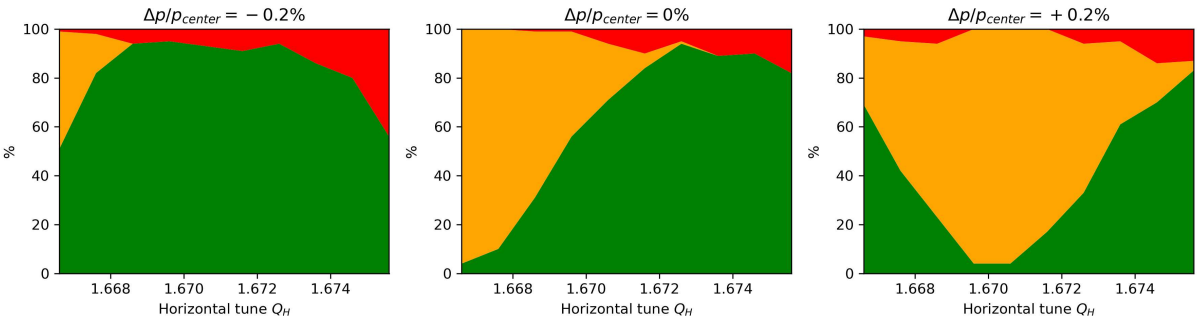

Figure 4.6.: Extraction diagram for a tune scan at different momentum offsets

As expected, a negative momentum offset (left) moves the particles further away from resonance, which corresponds to a shift of the on-momentum situation to the left and thus to a reduction of the early resonance losses. A stable plateau with high extraction efficiencies is established.
A positive momentum offset (right) shifts the plot to the right, which worsens the extraction efficiency. The resonance moves[3] from $Q_H = 1.6666$ to around 1.67.

[3]The fact that the resonance shift is not equivalent to the calculated value $\Delta Q = Q' \frac{\Delta p}{p} = 2 \cdot 10^{-3}$ confirms that the matched MAD-X chromaticity is not the chromaticity 'felt' by that particles. Thus, the corrections explained in 3.1.1 are necessary.

This first simulation shows that the particle extraction can be improved by superimposing an additional negative momentum offset to an off-tune scenario. Because of this, the tune scan was re-done for different MXR strengths with an applied momentum offset of -0.2%, resulting in the extraction diagrams shown in Figure 4.7.

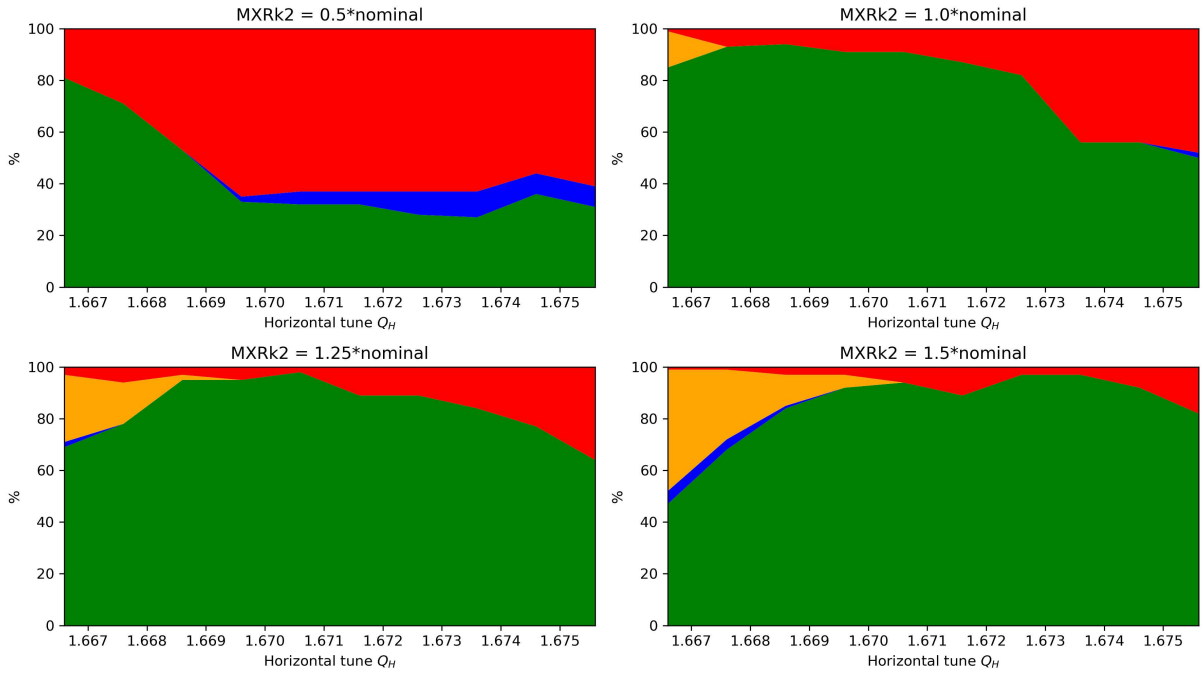

Figure 4.7.: Extraction diagram for a tune scan at different MXR strengths for the Hybrid scenario

Compared to the off-tune, on-momentum scenario in Figure 4.4, the additional momentum offset leads to a further improvement of the extraction efficiency and to a wider plateau.
For the Hybrid scenario, a plateau at above 90% extraction efficiency is established for all sextupole strengths but the lowest, where the spiral step is too small and the losses due to the width of the septum decrease the extraction efficiency. The highest MXR strength results in the best outcome. However, the achievable magnetic field is limited by the hardware of the magnet itself and the current and thus the strength should be chosen as low as possible. Nevertheless, also 125% of the nominal MXR strength value lead to a broad plateau at above 90% efficiency without any major losses and is thus a proper RF KO candidate.

4.4. Moving the electrostatic septum wall

For testing purposes, it was simulated how the position of the ESE wall impacts the extraction efficiency. For this, the position of the ESE wire remains unchanged at $x = -35\,\text{mm}$, but the aperture of the other side of the ESE chamber is changed. The nominal position of the ESE wall is $x = 72.4\,\text{mm}$. The simulation is performed for the nominal ESE position and for a displacement of -10 mm, -20 mm and -25 mm.
Figure 4.8 shows the resulting extraction diagram for the Hybrid scenario with $\frac{\Delta p}{p} = -0.2\%$, $Q' = -1$ and a MXR strength of 125% of the nominal value. The here introduced black area represents the losses at the wall of the ESE on the opposite side of the ESE wire.

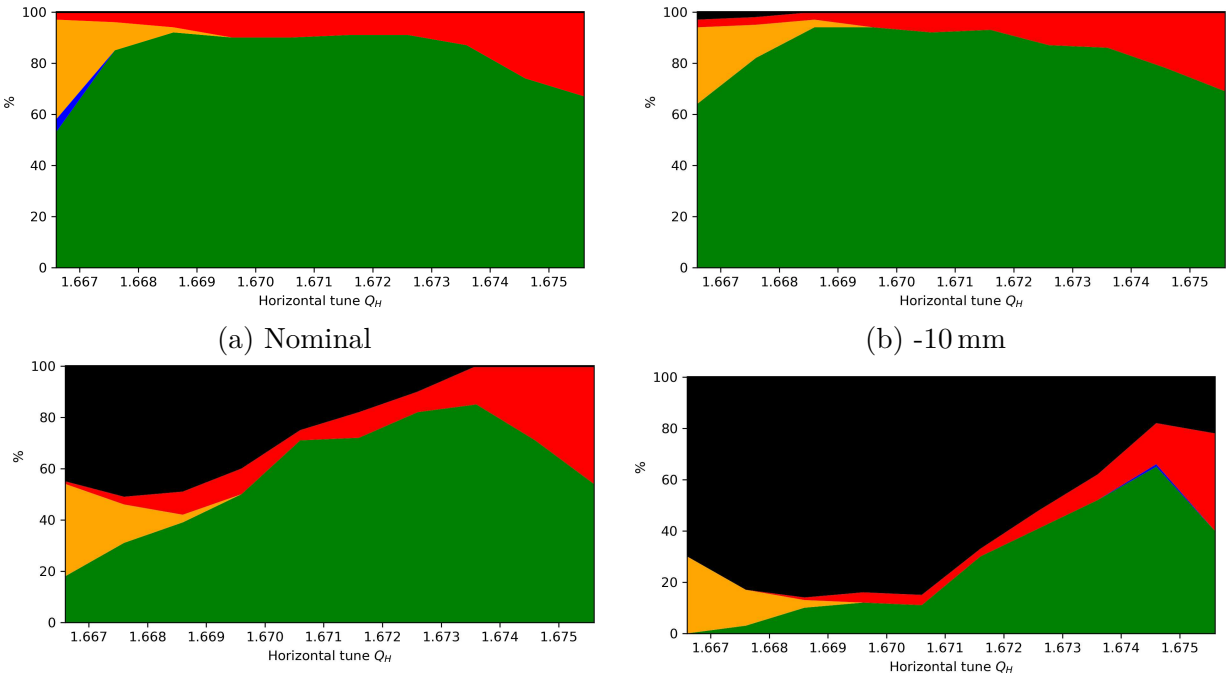

(a) Nominal

(b) -10 mm

(c) -20 mm

(d) -25 mm

Figure 4.8.: Extraction diagram for different displacements of the ESE wall

The ESE wall losses are increased when the ESE wall is moved inwards. This is the expected behaviour as the displacement decreases the available aperture for the betatron oscillations and thus more particles hit the wall and are lost.
Additionally, these losses destroy the plateau with a good extraction efficiency present at the nominal case and a distinct peak is evolving.

A displacement of -20 mm (sub plot 4.8c) is similar to the conditions of the ESE installation at the National Centre for Oncological Hadron-therapy (CNAO), where the septum is shifted 20 mm inwards with respect to the design orbit. Measurements of the extraction efficiency for different tunes confirms the presence of a sharp maximum peak, which is in accordance to the results of the simulation.
For RF KO implementation at CNAO, it is foreseen to minimize the ESE wall losses by using a orbit corrector or an angle bump at this location.[33]

5. Promising candidates for Radio Frequency Knockout

In this chapter, the results gathered from the parameter scans shown in the last chapter are put together to find promising sets of parameter for RF KO extraction. The two best candidates are discussed below.

5.1. Knockout candidate 1

As shown in the last chapter, the Hybrid scenario (off-tune and an additional off-momentum) produces the most promising results in terms of meeting the defined requirements.
Thus, the first candidate for RF KO extraction (denoted as *KOE 1*) is a Hybrid-type candidate with the parameter set as listed in Table 5.1.

Table 5.1.: Parameter for *KOE 1*

Parameter	**Value**
Horizontal tune Q_H	1.6706
Horizontal chromaticity Q'_H	-1
Strength of the resonant sextupole S	$1.25 \cdot 8.65 = 10.813$
Central momentum offset $\frac{\Delta p}{p}_{\text{center}}$	-0.2%

As one requirement of choosing a candidate for RF KO is the stability of the used setpoint, a parameter scan of the tune, the chromaticity, the strengths of the resonant sextupole and the momentum offset is performed around the setpoint. During the variation of one parameter, all the other mentioned variables are kept at their default values shown in Table 5.1. The extraction diagrams for the four parameter scans are shown in Figure 5.1.

All four diagrams confirm the plausibility of the parameter choice foe *KOE 1*, as the chosen working point is always located on a plateau of the extraction efficiency at around

the maximum value. Thus, small changes of a parameter (e.g. due to current ripples or wrong magnet settings) have got only a negligible impact on the extraction efficiency of RF knockout, which means that the chosen parameter setpoint of *KOE 1* is a suitable candidate for RF KO extraction.

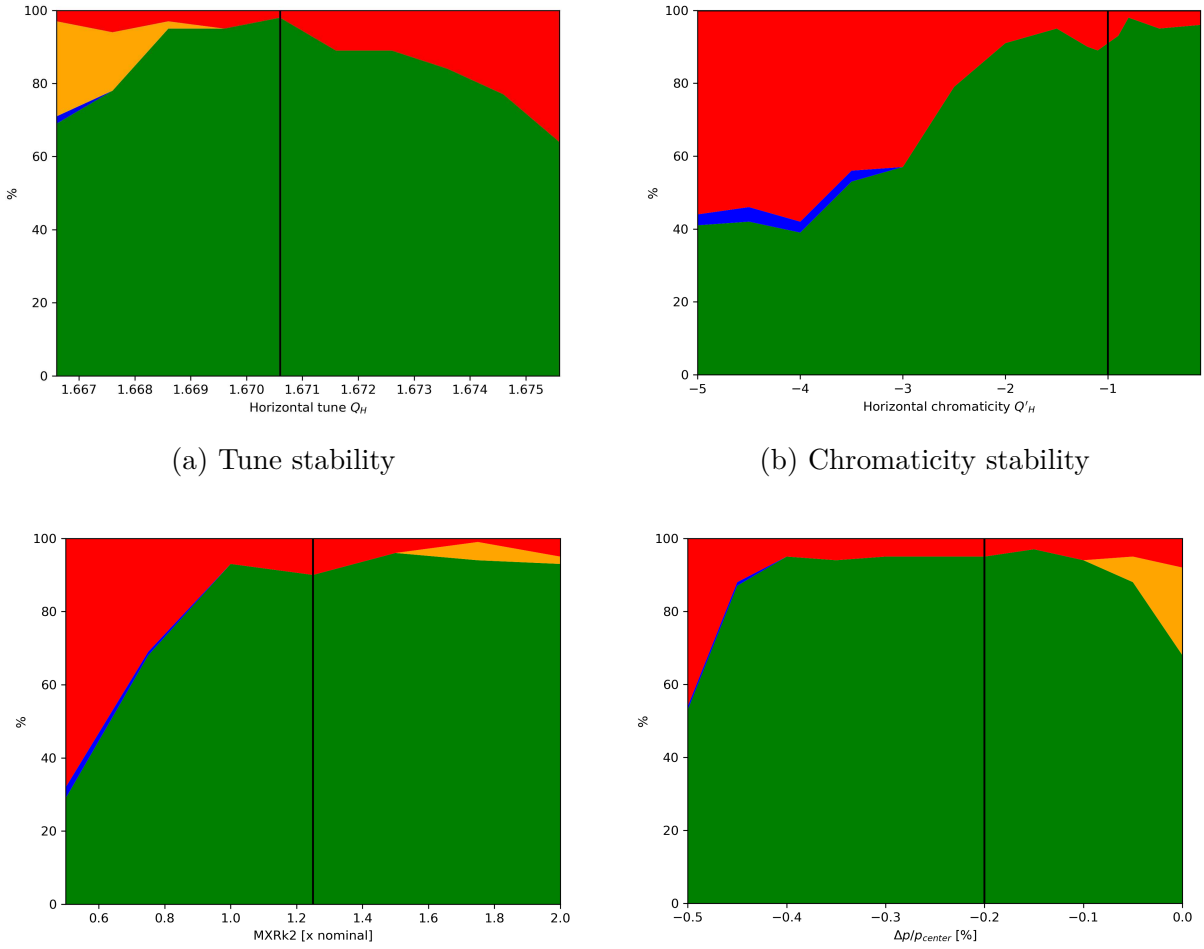

(a) Tune stability

(b) Chromaticity stability

(c) MXR stability

(d) Momentum offset stability

Figure 5.1.: Stability of *KOE 1* under parameter variation. The vertical black lines denote the respective parameter value chosen for *KOE 1*.

To investigate the requirement on the spiral step of the particles at extraction, the phase space at the ESE is plotted for all extracted particles in Figure 5.2. Additionally, also the particle momentum over the extraction turn number and over the particle position is shown for a better understand of the extraction mechanism.

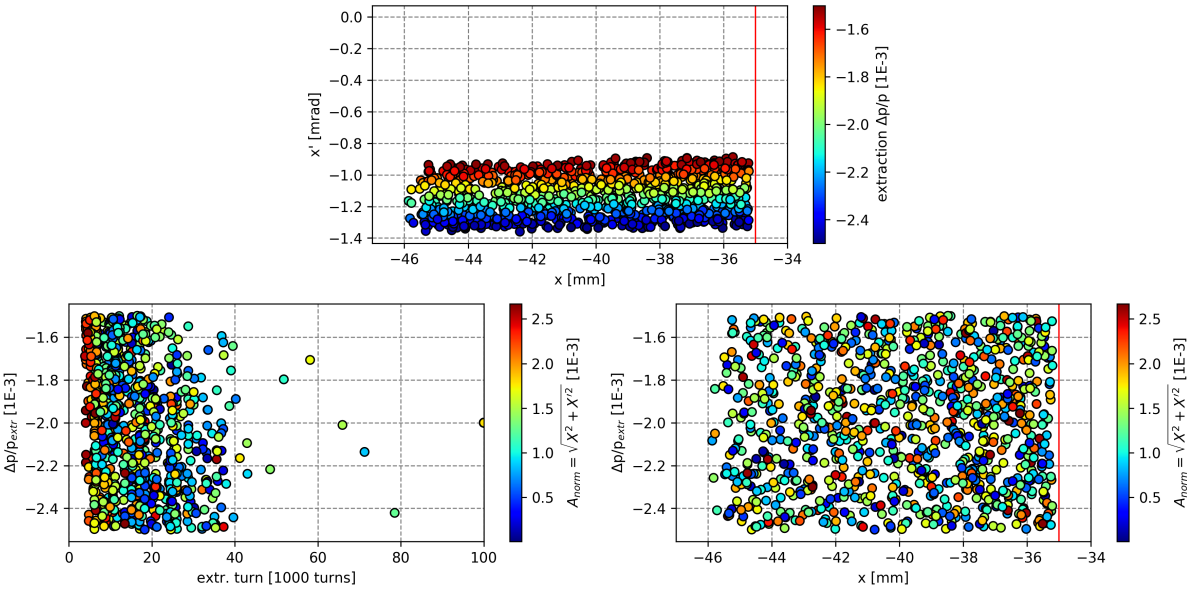

Figure 5.2.: Results of the KOE1 simulation
Top: Phase space of the extracted particles at the ESE, color-coded particle momentum
Bottom left: Particle momentum vs. extraction turn number, color-coded normalized particle amplitude
Bottom right: Particle momentum vs. position at extraction, color-coded normalized particle amplitude

The phase space shows that the spiral step is a little bit above 10 mm, which perfectly meets the requirements. As the extracted particles are amplitude-selected, the spiral step is independent of the particle momentum, which is also conformed by the bottom right plot of Figure 5.2. Due to the randomness of the kick, the extraction turn number does not correlate with the particle momentum or the particle amplitude. Only the particle with the highest initial amplitude (red points in the bottom left diagram) seem to be extracted at the very beginning of the process, as they are already very close to resonance. All other amplitudes are extracted in random order, as no sorting is visible in the plots.
Furthermore, it can be concluded from the bottom left diagram that the kick strength of the knockout exciter is too strong, as most particles are extracted already after 40% of the extraction process. This can be easily improved by decreasing the amplitude of the noise applied on the kicker, but the optimisation of the knockout excitation itself is not in the scope of this thesis.
All three plots of Figure 5.2 differ strongly from the reference plot for betatron core ex-

traction in Figure 3.9. This difference is further investigated in section 5.1.1.

Analogously to betatron core extraction, the phase space of the last 1000 turns before extraction is plotted also for RF KO in Figure 5.3.

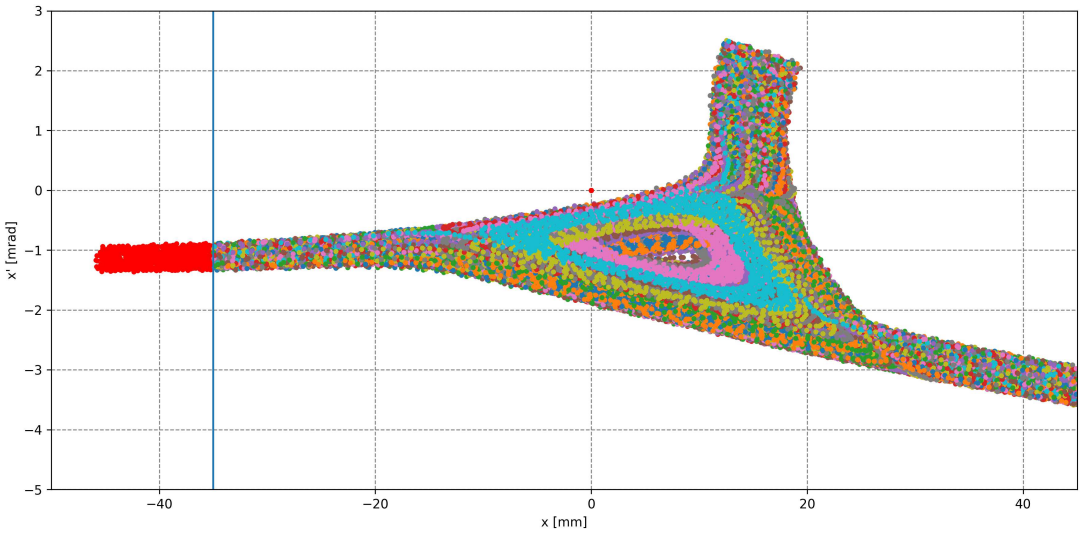

Figure 5.3.: Phase space at the ESE for the last 1000 turns before extraction. Each color represents one particle, the ESE wire position is marked as vertical line and the extracted particles are shown in red.

The third-order resonance triangles are similar to the ones for betatron core extraction in Figure 3.10. However, the random kick strengths lead to a 'blurred' shape of the triangles. Additionally, the Hardt condition is not fulfilled for the *KOE 1* settings. Thus, the separatrices for particles with different momenta do not overlap, which leads to a broader extraction branch of the separatrix and a wider angular distribution.

5.1.1. Comparison to betatron core extraction

In this section, the different extraction distributions for betatron core extraction and the first candidate for RF KO are compared and the differences as well as the similarities are pointed out.
The phase space distribution of the extracted particles at the electrostatic septum is shown in Figure 5.4. The squares denote the betatron core extraction, whilst the circles represent the *KOE 1* particles.

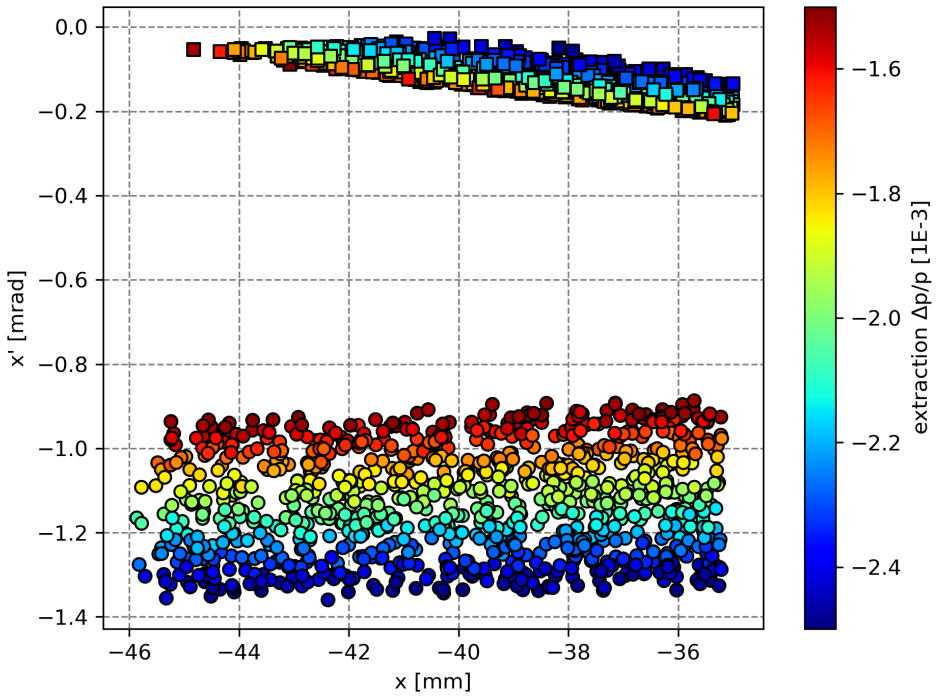

Figure 5.4.: Comparison of the phase space at the ESE between betatron core extraction (squares) and *KOE 1* (circles)

As explained in the last section, breaking the Hardt condition leads to an almost three times broader angular distribution for *KOE 1* compared to betatron core extraction. While the center of gravity of the particle position is similar for both extraction methods, there is a big discrepancy in the angular center of gravity, as the betatron core extraction leads to particles with angles of almost 0 mrad, while RF KO shifts the central angle to 1.1 mrad. However, this difference can be easily corrected by adjusting the kick of the electrostatic septum for *KOE 1* so that the resulting overall angle for both scenarios is the same again. Another interesting observation is that the correlation between particle momentum and angle is different for the two extraction mechanisms. For betatron core extraction, a higher particle momentum corresponds to a lower angle x', which is the opposite to the RF KO extraction.

Additionally, the spiral step is the same for all momenta for *KOE 1*, while it strongly depends on the momentum for betatron core extraction. This can be explained by taking into account that according to Figure 3.9, a lower particle momentum is correlated to an earlier extraction and thus they have got less time to increase the amplitude of the 'jump-

ing' from one branch of the separatrix to the other. This leads to the observed reduced spiral step for low momentum particles with betatron core extraction.
On the other hand, there is no correlation between extraction turn number and particle momentum for RF KO and therefore no dependency of the spiral step on the momentum.

The parameter of the two different extraction distributions are summarized in Table 5.2. The values confirm the points discussed above about the differences in the distribution.
By calculating the center of gravity for the top and bottom 10% of the particles with respect to the momentum, a shift vector in momentum space can be determined by subtracting the high-momentum central values from the low-momentum ones. If this shifting vector is divided by the momentum spread, the intrinsic dispersion of the distributions at the septum can be evaluated with equation 5.1.

$$\begin{pmatrix} D_x \\ D'_x \end{pmatrix}_{\text{distribution}} = \frac{1}{\left(\frac{\Delta p}{p}\right)_{\text{spread}}} \begin{pmatrix} \Delta x \\ \Delta x' \end{pmatrix}_{\text{shift}} \tag{5.1}$$

The thus calculated dispersion values for both distributions are also shown in Table 5.2. The almost vanishing value of D_x for *KOE 1* corresponds to the fact the spiral step is independent of the particle momentum for RF KO. It is further worth mentioning that the absolute value of D'_x correlates to the different angle spans of the distribution, while its different signs represent the fact that the order of the extracted particles with regard to the particle momentum is differing for *KOE 1* and betatron core extraction.

Table 5.2.: Comparison of the extracted particle distribution at the ESE between *KOE 1* and betatron core extraction (MIN)

	KOE 1	**MIN**
Position center x_{CoG}	-39.61 mm	-38.41 mm
Angle center x'_{CoG}	-1.13 mrad	-0.12 mrad
Position span x_{span}	10.66 mm	9.37 mm
Angle span x'_{span}	0.47 mrad	0.18 mrad
D_x	-0.13 m	-1.96 m
D'_x	0.39 rad	-0.05 rad

5.1.2. Tracking to magnetostatic septum

To investigate how the different distributions at the electrostatic septum affects the movement of the particles during further extraction, a tracking from the electrostatic septum to the magnetostatic septum (MST) is performed. The distributions at the ESE for *KOE 1* and MIN extraction are taken as initial particles for the further tracking. The starting point of the main ring lattice is cycled to the ESE and the MST is used as observation point.
To set up the extraction process correctly, the distribution parameter listed in Table 5.2 are used as initial values for x, x', D_x and D'_x in the MAD-X TWISS process.
Additionally, the kick which is applied on the particles by the ESE has to be adapted to get the same results for both cases. As the angle center for *KOE 1* is one mrad lower than the one for MIN extraction, the ESE kick strength has to be decreased by this amount to guarantee that the kick affects both distributions identically.
The resulting phase space of *KOE 1* and MIN extraction at the magnetostatic septum is compared in Figure 5.5.

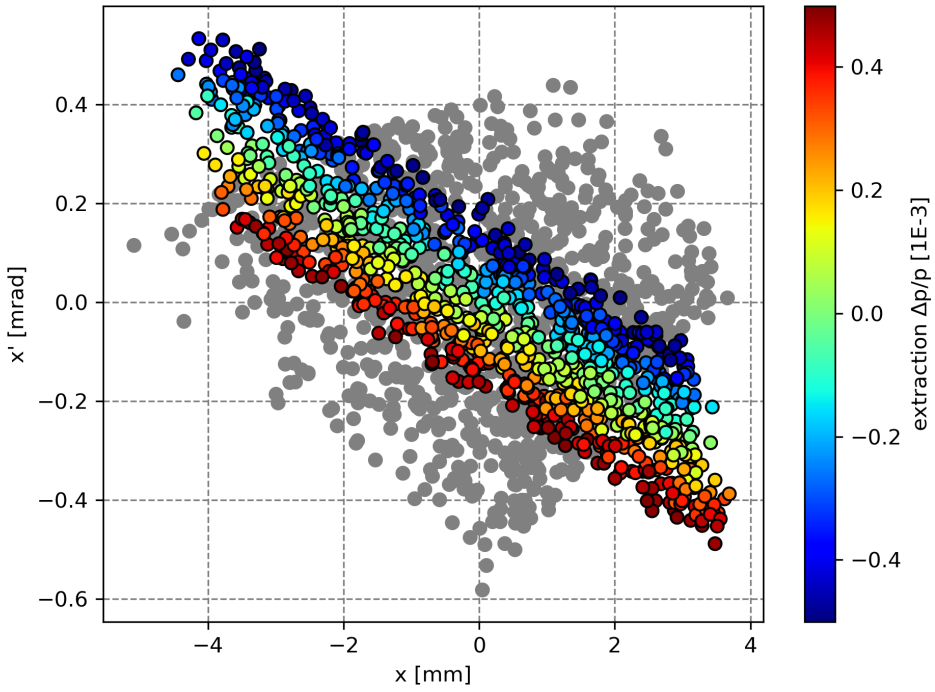

Figure 5.5.: Comparison of the phase space at the MST between betatron core extraction (grey) and *KOE 1* (colour)

As the particles leave the coordinate system of the Main Ring at the MST and enters the linear coordinate system of the High Energy Beam Tranfer Line (HEBT), both distributions have to be centered at the MST, which is done by shifting the particle coordinates x, x' and pt so that the center of gravity for the distribution is zero for all three parameter. Thus, Figure 5.5 shows the centered distributions.
The width in position and angle of the extracted particle distribution is identical for both extraction methods. Additionally, the 'tilting' of the distribution on phase space is also comparable. However, the shape is clearly different, as RF KO leads to a narrower distribution.
However, the different shape is irrelevant for commissioning, as the identical width implements that no problems due to scraping the aperture are expected. The shape of the extracted particles in phase space can be adjusted to the one for betatron core extraction via adapting the dispersion vector.

5.1.3. Further tracking of the beamline

For a final confirmation of the similar behaviour of betatron core and RF KO extraction also in the down-stream parts of the beamline, the centered distributions at the magnetostatic septum is tracked further to the first SFX monitor of the HEBT (EX-00-000-SFX). The results are shown in Figure 5.6.

At this point, the position and angle span of the *KOE 1* distribution is smaller than for betatron core extraction, as well as the shape of the distribution is more compressed. Additionally, a slight mixing of the different particle momenta can be observed, which is not visible for the betatron core extraction.
To explain this difference, the dispersion-removed phase space for both distributions is plotted in Figure 5.7. For this, the dispersive part of position and angle are removed by equation 4.3.
The comparison shows that the order with respect to particle momentum is reversed for *KOE 1*. The low-momentum particles are at low positions, while the opposite situation of low-momentum particles at high positions is present for betatron core extraction. This momentum reversion already appeared at the ESE, as discussed above.
From this dispersion-free starting point, the particles are shifted in momentum space by the dispersion vector. The dispersion at the position of the regarding SFX is

$$\begin{pmatrix} D_x \\ D'_x \end{pmatrix}_{\text{SFX}} \approx \begin{pmatrix} -5.6\,m \\ 0.1\,rad \end{pmatrix}. \tag{5.2}$$

Thus, particles with a negative momentum (blue) are shifted to positive positions (i.e. to the right), while positive-momentum particles are shifted to negative positions (to the left)

by dispersion. The shifting is visualized by black lines for some particles in Figure 5.7.
For betatron core extraction, this leads to a broadening of the distribution in phase space. As the momentum order without dispersion is reversed for *KOE 1*, the dispersive shifting produces a narrowing and even a mixing of the distribution.
This means that the particle mixing in Figure 5.6 for *KOE 1* can be explained by the reversed initial distribution with respect to the particle momentum and the dispersive shifting. Thus, the shape can be easily adjusted by changing the dispersion in the HEBT.

In summary, it can be stated that the analysed candidate for RF KO leads to similar distributions at the ESE, the MST and also the first SFX as betatron core extraction. The spread in position and angle are comparable, so aperture-related problems are not expected. The different shapes of the distributions can be adjusted by changing the dispersion vector in the HEBT.

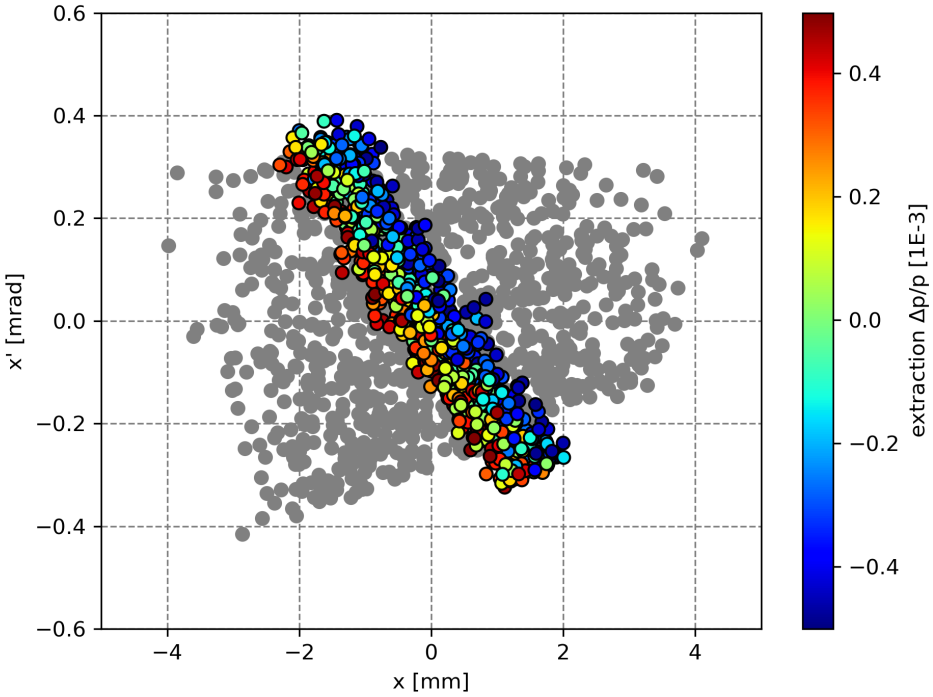

Figure 5.6.: Comparison of the phase space at the first SFX of the High Energy Beam Transfer Line (HEBT) between betatron core extraction (grey) and *KOE 1* (colour)

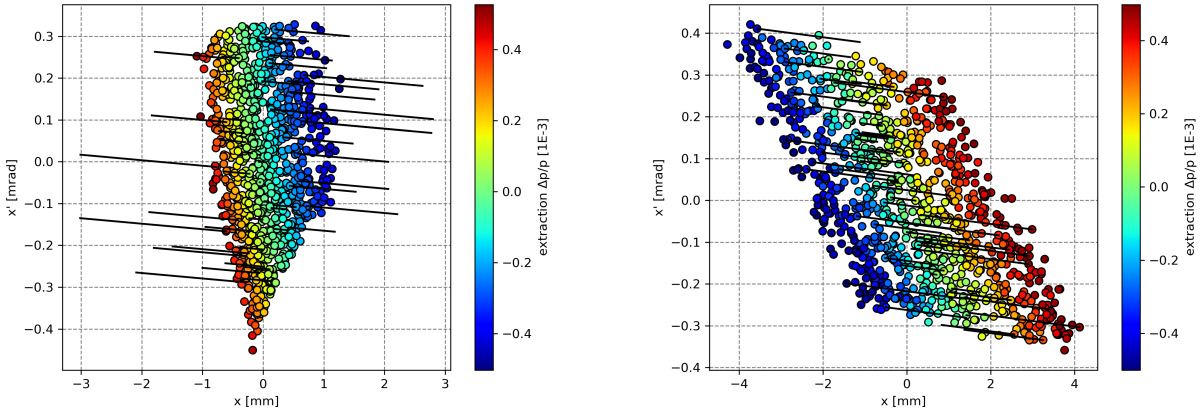

(a) Betatron core extraction

(b) *KOE 1*

Figure 5.7.: Dispersion-cleared phase space at the first SFX in the High Energy Beam Transfer Line for both extraction scenarios

5.2. Knockout candidate 2

After the simulations for the Hybrid-type *KOE 1*, the corresponding off-tune, on-momentum candidate was analysed closer. For this, the momentum offset of *KOE 1* has to be converted to a tune shift via the definition of the chromaticity 4.4. However, it has to be taken into account that off-momentum particles feel a different chromaticity than the set value, as explained in section 3.1.1. Because of this, the set tune and chromaticity value for *KOE 1* ($Q = 1.6706$, $Q' = -1$) cannot be directly used to calculate the equivalent tune shift, but a Fourier analysis has to be performed to extract the 'real' chromaticity and tune. The analysis yields a tune value of $Q = 1.6735$ and a chromaticity value of $Q' = -2.1$, which results in the parameter settings for the off-tune, on-momentum candidate *KOE 2* as summarised in Table 5.3.

Table 5.3.: Parameter for *KOE 2*

Parameter	**Value**
Horizontal tune Q_H	1.6735
Horizontal chromaticity Q'_H	-2.1
Strength of the resonant sextupole S	$1.25 \cdot 8.65 = 10.813$
Central momentum offset $\frac{\Delta p}{p}_{\text{center}}$	0%

With this new settings, the simulations of *KOE 1* are repeated and the resulting extracted particle distribution analysed. The results of the analysis is shown in Figure 5.8.

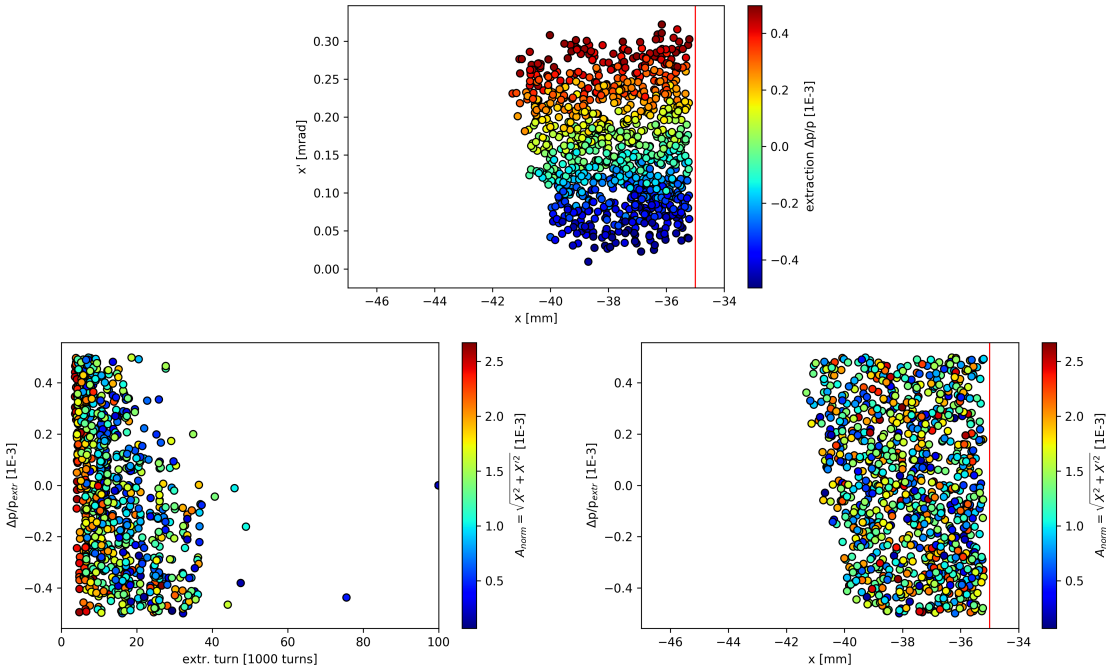

Figure 5.8.: Results of the KOE2 simulation
Top: Phase space of the extracted particles at the ESE, color-coded particle momentum
Bottom left: Particle momentum vs. extraction turn number, color-coded normalized particle amplitude
Bottom right: Particle momentum vs. position at extraction, color-coded normalized particle amplitude

The results of the simulation are similar to the ones for *KOE 1* (see Figure 5.2). The main difference is that the spiral step is only 6 mm for *KOE 2* instead of more than 10 mm for *KOE 1*. Additionally, the average extraction turn number is lower than for *KOE 1*, which means that the particles get extracted earlier.
Despite these differences, the shape and the dimensions of the extracted distribution are similar for both candidates.

To investigate the origin of the reduced spiral step, the phase space at the electrostatic septum for the last 1000 turns before extraction is plotted and compared to *KOE 1*, as shown in Figure 5.9.

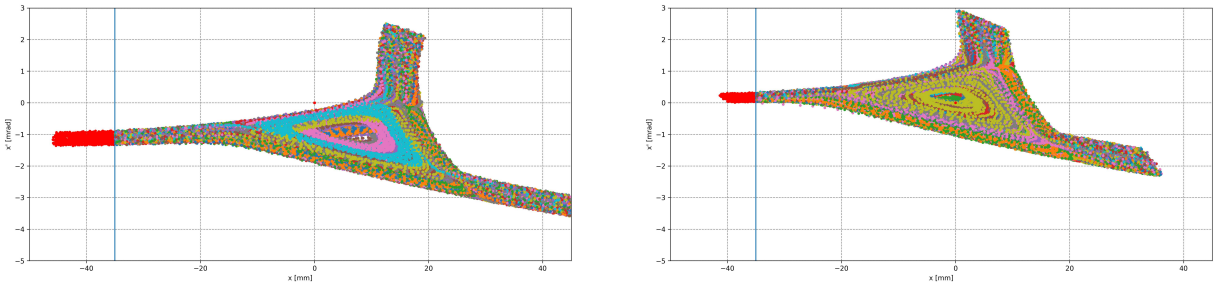

(a) *KOE 1* (b) *KOE 2*

Figure 5.9.: Phase space at the ESE for the last 1000 turns before extraction for *KOE 1* and *KOE 2*

As the dispersion at the septum is different for both settings, the phase space distribution is shifted differently for *KOE 1* and *KOE 2*. For *KOE 2*, the triangle is closer to the ESE wire, which explains why the particles are extracted earlier. Because of this shorter extraction time, the growing time of the particle jumping amplitude along the separatrix branches is limited and the spiral step is thus smaller. Therefore, it is most likely that the reduced spiral step can be related to the changed dispersion.

For a more accurate comparison, the separatrix at the resonant sextupole and the electrostatic septum is reconstructed for both candidates. For this, a procedure similar to the reconstruction of the Steinbach diagram in section 3.1 is used by tracking a grid of particles and checking if and at which turn number the particles are extracted. Prior to the plotting, the dispersive part of position and angle is removed and normalised coordinates (X, X') are used. The resulting stable triangle of this analysis is shown in Figure 5.10 for both *KOE 1* and *KOE 2*.

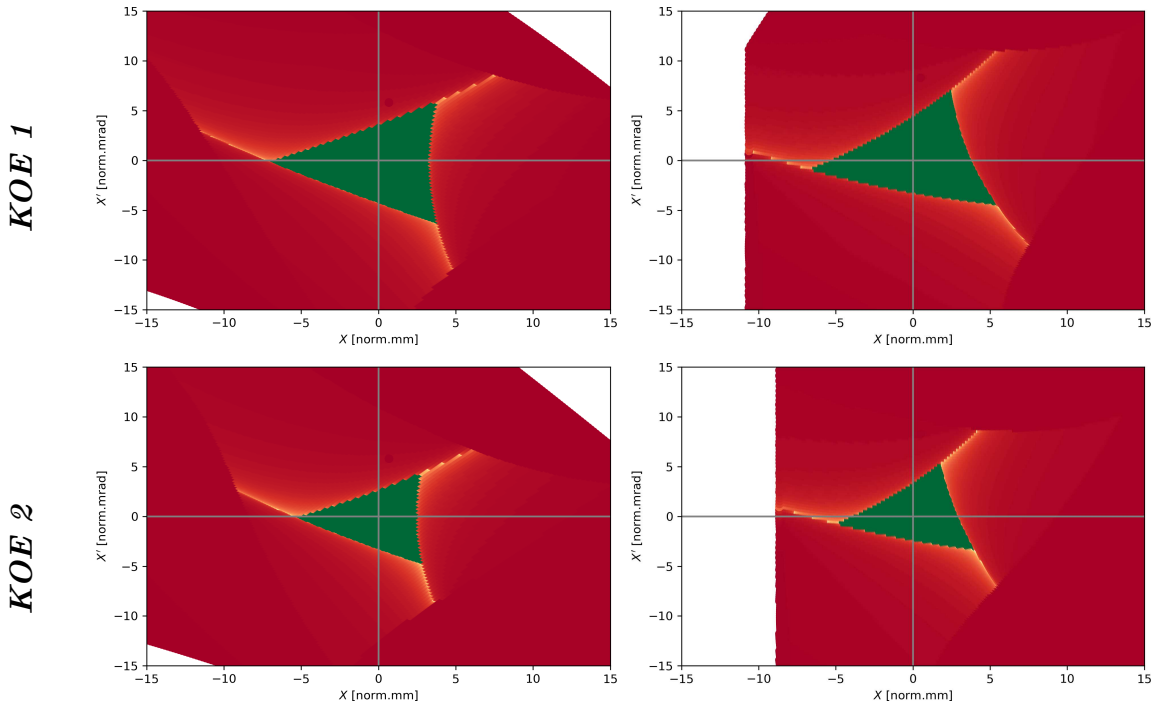

(a) Resonant sextupole (b) Electrostatic septum

Figure 5.10.: Simulated separatrix at MXR and ESE for *KOE 1* (*top*) and *KOE 2* (*bottom*)

For both observation points, the theoretically expected orientation of the stable triangle and the rotation between MXR and ESE as shown in Figure 2.7 is reproduced by the simulation for both candidates.[1] However, the area of the stable triangle for *KOE 2* is significantly smaller than for *KOE 1*. Comparing with the theoretically expected value, it is discovered that *KOE 2* area is very close to the acceptance calculated with equation 2.33, while the stable area for *KOE 1* is almost 90% bigger than it should theoretically be. This deviation from theory is not fully understood yet and has to be further investigated.

Beside this smaller stable triangle and the reduced spiral step, the extraction process leads to similar results as the *KOE 1* candidate. Further tracking to the magnetostatic septum and the first SFX of the HEBT leads to results similar to the Hybrid case *KOE 1* discussed above. Because of this, both *KOE 1* and *KOE 2* are acceptable candidates for RF KO extraction. However, one has to keep in mind that the spiral step for *KOE 2* is smaller than the required 10 mm.

[1] However, both axes are inverted because of the changed sign of δQ, compared to the value used to plot Figure 2.7.

6. Summary and outlook

After the simulations described above, it can be concluded that the MedAustron synchrotron is capable of extracting via radio frequency knockout, as experimentally demonstrated in [34]. The extraction efficiency prior to the optics optimizations proposed in this thesis was 32%.
The extraction mechanism can be reproduced accordingly with MADX simulations of a transverse kicker with noise as excitation pattern.
To reach a plateau at an acceptable extraction efficiency, the strength of the resonant sextupole has to be increased by 25% from the nominal value. A horizontal chromaticity near $Q'_H = -1$ is favourable for the extraction quality. The scenario which meets the requirements best is the Hybrid case (*KOE 1*), where the extraction process is executed both off-tune and off-momentum.
Additionally, also the corresponding off-tune, on-momentum scenario (*KOE 2*) results in a satisfying outcome, when the tune shift is calculated from the Hybrid candidate via using the chromaticity. However, one has to keep in mind that the off-momentum particles feel a chromaticity different to the set value. The real chromaticity value can be obtained by a Fourier analysis of the position over turn number.
Both *KOE 1* and *KOE 2* are suitable candidates for RF KO with a high extraction efficiency, even for small variations of tune, chromaticity or the strength of the resonant sextupole. The spiral step for *KOE 1* is near to the target value of 10 mm, while *KOE 2* results in a spiral step of only 6 mm.

A possible future continuation could focus on two different topics. Firstly, the difference between *KOE 1* and *KOE 2* should be further investigated. Although both should describe similar extraction conditions, the separatrix as well as the spiral step is different for the two candidates. Closely related to this topic is the analysis on why the real chromaticity is different to the set value for off-momentum particles.
Secondly, the impact of the excitation pattern such as sawtooth or sinusoidal instead of noise on the extraction process should be analysed. The main problem about setting a time-dependent pattern is that the MADX update macro cannot access the longitudinal position (i.e. time) of each particle as variable, but only the turn number. This implies that no particles pass the kicker before or after the reference particle and the same kick is applied to all particles. This is obviously not the case and thus the MADX update macro

cannot model reality sufficiently.
One possibility so solve this problem and to address the particle time directly is to use a map tracking approach to create a PTC map of the region of interest and track the particles with Python instead of MADX. This concept was originally developed by Velotti et al. to simulate crystal-beam interaction and can be perfectly used for a more flexible tracking as it is necessary for implementing different time-dependent excitation patterns in the particle tracking routine.[35]
Additional future work will also include a study of the longitudinal beam dynamics for bunched beams and parameter optimisation with respect to the spill quality, especially intensity spill ripples.

List of Figures

1.1. The MedAustron accelerator complex 1

2.1. Local cylindrical coordinate system 6
2.2. The shape of the phase space ellipse, depending on the Twiss parameter . . 12
2.3. Resonance diagram with resonances up to third order 13
2.4. Contour plot of the unperturbed circular and the superimposed sextupole component of the Kobayashi Hamiltonian 15
2.5. Contour plot of the Kobayashi Hamiltonian with separatrices 15
2.6. The stable triangle at the resonant sextupole and the coordinates of the four fixed points 16
2.7. The rotation of the stable triangle in phase space 17
2.8. Separatrices for three particles with different momentum offsets 18
2.9. Superimposed separatrices for particles with different $\frac{\Delta p}{p} < 0$ 19
2.10. Steinbach diagram near a resonant tune Q_{res} 20
2.11. Steinbach diagram for betatron core driven extraction 22
2.12. Single particle phase space for betatron core driven extraction 22
2.13. Steinbach diagram for RF knockout driven extraction 23

3.1. Simulated Steinbach diagram for 10^4 particles and 1000 turns 26
3.2. Simulated and theoretical Steinbach diagram at the resonant sextupole . . 27
3.3. Relative chromaticity error for different tune and chromaticity settings . . 29
3.4. Steinbach diagram with calculated chromaticity values 30
3.5. Steinbach diagram for different tunes 31
3.6. Steinbach diagram for different chromaticities 32
3.7. Steinbach diagram for different strengths of the resonant sextupole 33
3.8. Initial distribution for betatron core simulation 36
3.9. Results of the betatron core simulation 37
3.10. Horizontal phase space at the ESE for the last 1000 turns before extraction 38

4.1. Example of an extraction diagram 41
4.2. Results of the proof of principle simulation of RF KO 43
4.3. Extraction diagram for a scan of the momentum offset at different MXR strengths for the on-tune, off-momentum scenario 46

4.4. Extraction diagram for a tune scan at different MXR strengths for the off-tune, on-momentum scenario 47
4.5. Extraction diagram for a tune scan at different chromaticity values for the off-tune, on-momentum scenario 48
4.6. Extraction diagram for a tune scan at different momentum offsets 49
4.7. Extraction diagram for a tune scan at different MXR strengths for the Hybrid scenario 50
4.8. Extraction diagram for different displacements of the ESE wall 51

5.1. Stability of *KOE 1* under parameter variation 54
5.2. Results of the KOE1 simulation 55
5.3. Horizontal phase space at the ESE for the last 1000 turns before extraction 56
5.4. Comparison of the phase space at the ESE between betatron core extraction (squares) and *KOE 1* (circles) 57
5.5. Comparison of the phase space at the MST between betatron core extraction (grey) and *KOE 1* (colour) 59
5.6. Comparison of the phase space at the first SFX of the High Energy Beam Transfer Line (HEBT) between betatron core extraction (grey) and *KOE 1* (colour) 61
5.7. Dispersion-cleared phase space at the first SFX in the High Energy Beam Transfer Line for both extraction scenarios 62
5.8. Results of the KOE2 simulation 63
5.9. Phase space at the ESE for the last 1000 turns before extraction for *KOE 1* and *KOE 2* 64
5.10. Simulated separatrix at MXR and ESE for *KOE 1* (*top*) and *KOE 2* (*bottom*) 65

Bibliography

[1] M. Benedikt and A. Wrulich. MedAustron—Project overview and status. *European Physical Journal Plus*, 126:1–11, 07 2011.

[2] G. Feldbauer. *Extraction methods for the MedAustron Synchrotron*. 2011. Diploma Thesis at Vienna University of Technology.

[3] E. Sargsyan. *MedAustron Injector - Design Report*. 2010. Functional specifications, Version 1.0.

[4] A. Wastl. *Development of the orbit correction procedure and simulations on rf-noise driven slow resonant extraction of MedAustron synchrotron*. 2013. Master Thesis at Vienna University of Technology.

[5] P.J. Bryant and U. Dorda. *MedAustron MEBT design report*. 2010. Engineering Note, Version 1.1.

[6] P.J. Bryant and U. Dorda. *MedAustron Synchrotron design report*. 2010. Engineering Note, Version 1.1.

[7] P.J. Bryant and U. Dorda. *MedAustron HEBT design report*. 2010. Engineering Note, Version 1.4.

[8] Accelerator Complex Study Group. *Proton-Ion Medical Machine Study (PIMMS) Part I*. CERN, 1999.

[9] S. Savazzi, E. Bressi, G. Debernardi, L. Falbo, V. Lante, C. Priano, M. Pullia, P. Meliga, and G. Russo. Implementation of RF-KO extraction at CNAO. In *10th Int. Particle Accelerator Conf., IPAC2019, Melbourne, Australia*, 2019.

[10] S. Sato, T. Furukawa, and K. Noda. Development of intensity control system with RF-knockout at the HIMAC synchrotron. In *Proceedings of EPAC 2006, Edinburgh, Scotland*, 2006.

[11] Y. Hatano, Y. Katsumura, and A. Mozumder. *Charged Particle and Photon Interactions with Matter: Recent Advances, Applications, and Interfaces*. CRC Press, 2010.

[12] K. Noda, T. Furukawa, S. Shibuya, T. Uesugi, M. Muramatsu, M. Kanazawa, E. Takada, and S. Yamada. Advanced RF-KO slow-extraction method for the reduction of spill ripple. *Nuclear Instruments and Methods in Physics Research*, 492:253–263, 10 2002.

[13] M. Conte and W.W. MacKay. *An Introduction to the Physics of Particle Accelerators*. World Scientific, 2008.

[14] P.J. Bryant and K. Johnsen. *The Principles of Circular Accelerators and Storage Rings*. Cambridge University Press, 2005.

[15] S. Turner (Ed.). *CERN Accelerator School - Proceedings of the Fifth General Accelerator Physics Course, Vol. I*. CERN, 1994.

[16] W. Hardt. *Ultraslow extraction out of LEAR (transverse aspects)*. CERN Internal Note PS/DL/LEAR Note 81-6.

[17] M. Pullia. *Transverse aspects of the slowly extracted beam*. 2000.

[18] F. Kühteubl. *Dynamic simulation of Main Ring ramping and extraction of the MedAustron synchrotron with MAD-X*. 2017. Bachelor Thesis at Vienna University of Technology.

[19] G. Feldbauer, M. Benedikt, and U. Dorda. Simulations of Various Driving Mechanisms for the 3rd Order Resonant Extraction from the MedAustron Medical Synchrotron, 2011.

[20] N. Carmignani, C. Biscari, M. Serio, G. Balbinot, E. Bressi, M. Caldara, M. Pullia, J. Bosser, and G. Venchi. Rf-knockout extraction system for the cnao synchrotron. In *Proceedings of IPAC'10, Kyoto, Japan*, 2010.

[21] J. Li and Y. Yuan. RF Excitation Parameters in Resonant Extraction. In *Proceedings of the 13th Symposium on Accelerator Physics (SAP 2017), Jishou, China*, 2018.

[22] T. Furukawa, K. Noda, M. Muramatsu, T. Uesugi, S. Shibuya, H. Kawai, E. Takada, and S. Yamada. Global spill control in RF-knockout slow-extraction. *Nuclear Instruments and Methods in Physics Research Section A: Accelerators, Spectrometers, Detectors and Associated Equipment*, 522:196–204, 04 2004.

[23] K. Mizushima, T. Shirai, T. Furukawa, S. Sato, Y. Iwata, K. Noda, and H. Uchiyama. Reduction of uncontrollable spilled beam in rf-knockout slow extraction. *Nuclear Instruments and Methods in Physics Research Section A-accelerators Spectrometers Detectors and Associated Equipment*, 606:325–329, 07 2009.

[24] H.J. Yao, G.R. Li, Q. Zhang, S.X. Zheng, X.L. Guan, and X.W. Wang. RF-knockout slow extraction design for XiPaf synchrotron. In *Proceedings of HB2016, Malmö, Sweden*, 2016.

[25] C. Schömers, E. Feldmeier, M. Galonska, T. Haberer, J. Horn, and A. Peters. First Tests of a Re-accelerated Beam at Heidelberg Ion-Beam Therapy Centre (HIT). In *Proceedings of the 8th International Particle Accelerator Conference (IPAC 2017): Copenhagen, Denmark*, 2017.

[26] T. Furukawa, T. Inaniwa, S. Sato, T. Shirai, Y. Takei, E. Takeshita, K. Mizushima, Y. Iwata, T. Himukai, S. Mori, S. Fukuda, S. Minohara, E. Takada, T. Murakami, and K. Noda. Performance of the NIRS fast scanning system for heavy-ion radiotherapy. *Medical physics*, 37:5672–82, 11 2010.

[27] F. Ebina, M. Umezawa, and K. Hiramoto. Improvement of extraction efficiency from a slow extraction synchrotron by applying the constant spiral step condition. *Nuclear Instruments and Methods in Physics Research Section A: Accelerators, Spectrometers, Detectors and Associated Equipment*, 685:1–6, 09 2012.

[28] L. Adler, A. De Franco, F. Farinon, N. Gambino, G. Guidoboni, C. Kurfürst, S. Myalski, M.T.F. Pivi, C. Schmitzer, I. Strasik, and A. Wastl. Synchrotron emittance analysis procedure at MedAustron. In *Proceedings of the 7th Int. Beam Instrumentation Conf. (IBIC2018), Shanghai, China*, 2018.

[29] A. Garonna, M. Kronberger, T. Kulenkampff, C. Kurfürst, F. Osmić, L. Penescu, M. Pivi, C. Schmitzer, P. Urschütz, and A. Wastl. Status of the Proton Beam Commissioning at the MedAustron Ion Beam Therapy Centre. In *Proceedings of the 6th International Particle Accelerator Conference (IPAC 2015): Richmond, Virginia, USA*, 2015.

[30] A. Garonna, F. Farinon, M. Kronberger, T.K.D. Kulenkampff, C. Kurfürst, S. Myalski, S. Nowak, F. Osmić, L.C. Penescu, M.T.F. Pivi, C. Schmitzer, P. Urschütz, and A. Wastl. Status of Proton Beam Commissioning of the MedAustron Particle Therapy Accelerator. In *Proceedings of the International Particle Accelerator Conference (IPAC'16), Busan, Korea*, pages 3176–3179, 2016.

[31] M.T.F. Pivi, L. Adler, A. De Franco, F. Farinon, N. Gambino, G. Guidoboni, G. Kowarik, M. Kronberger, C. Kurfürst, H.T. Lau, S. Myalski, S. Nowak, C. Schmitzer, I. Strasik, P. Urschütz, A. Wastl, and L. Penescu. Status of the Carbon Commissioning and Roadmap Projects of the MedAustron Ion Therapy Center

Accelerator. In *Proceedings of the 10th International Particle Accelerator Conference (IPAC2019): Melbourne, Australia*, 2019.

[32] M.G. Pullia, E. Bressi, L. Falbo, C. Priano, S. Rossi, C. Viviani, A. Garonna, M. Kronberger, T. Kulenkampff, C. Kurfürst, F. Osmic, L. Penescu, M.T.F. Pivi, C. Schmitzer, P. Urschütz, and A. Wastl. Betatron core driven slow extraction at cnao and medaustron. In *Proceedings of IPAC2016, Busan, Korea*, 2016.

[33] M. Pullia and L. Falbo. CNAO (private communication, January 2020).

[34] A. De Franco, L. Adler, F. Farinon, N. Gambino, G. Guidoboni, G. Kowarik, M. Kronberger, C. Kurfürst, S. Myalski, S. Nowak, M.T.F. Pivi, C. Schmitzer, I. Strasik, P. Urschütz, A. Wastl, and L. Penescu. Slow Extraction Optimization at the MedAustron Ion Therapy Center: Implementation of Front End Acceleration and RF Knock Out. In *Proceedings of the 9th International Particle Accelerator Conference (IPAC2018), Vancouver, BC, Canada*, 2018.

[35] F.M. Velotti, L.S. Esposito, M.A. Fraser, V. Kain, S. Gilardoni, B. Goddard, M. Pari, J. Prieto, R. Rossi, W. Scandale, L.S. Stoel, F. Galluccio, M. Garattini, and Y. Gavrikov. Septum shadowing by means of a bent crystal to reduce slow extraction beam loss. *Phys. Rev. Accel. Beams*, 22:093502, Sep 2019.

[36] H. Aiginger and K. Poljanc. *Script of "141.944 Teilchenbeschleuniger"*. Vienna University of Technology, 2005.

[37] H. Grote and F. Schmidt. *The MAD-X Program*. European Laboratory For Particle Physics, Geneva, Switzerland, 2017. User's Reference Manual, Version 5.03.06, `http://mad.web.cern.ch/mad/`.

[38] A. De Franco. private communication, Dezember 2019.

[39] J. Holmes, S. Henderson, and Y. Zhang. Transverse Beam Optics, Part I. In *Proceedings from USPAS Vanderbilt*, 2009.

[40] B. Holzer. Introduction in Transverse Beam Dynamics. In *Proceedings from CAS Prague*, 2014.

[41] M. Benedikt. *Lecture Notes of "141.944 Teilchenbeschleuniger"*. Vienna University of Technology, 2012.

Acknowledgements

There are many people who made a substantial contribution during the production process of this thesis and who I would like to thank at this point.
At first, I would like to express my sincere gratitude to my supervisor from university, Michael Benedikt, for his precious support and advice from defining the topics until the writing of the thesis.

Secondly, a big thank you to my supervisor from MedAustron, Andrea de Franco. It was a pleasure to work with you and to learn from your amazing experience in the field of accelerator physics.
Many thanks also to the ABP group at MedAustron for accepting me as part of the team and for always supporting me when I got stuck. A special thanks to Mauro Pivi for the interesting discussions during our office sharing and to Christoph Kurfürst for helping me with all sorts of administrative and physics-related problems.

I thank the colleagues Marco Pullia and Luciano Falbo from CNAO for the valuable technical exchange on RF KO technique and implementation at facilities designed after the PIMMS.
I would also like to say thank you to Matthew Fraser and Pablo Sota from the TE-ABT-BTP group at CERN for their warm hospitality during my trip to CERN and the many fruitful discussions about physics.

Last but not least, I would like to thank my family. You are always there for me and support all my choices in life, no matter whether good or not. Without you, I wouldn't be where I am now. Also a big thanks to my 'Fifth Wheel' group, my friends from 'Dancefire' and, of course, to my girlfriend Sarah for changing my life for the better.

Finally, everything that is left to be said is[1]:

[1] https://minimumble.thebookofbiff.com/tag/bison/

A. Basis structure of the MAD-X scripts

All simulations of this thesis were performed with MAD-X and analysed with Python 3.6. In introduction to working with MAD-X is not part of this thesis and can be found in [37]. The following enumeration provides only a quick overview on how a typical MAD-X script used for simulations is composed.

1. **Loading the MedAustron lattice files**: The definitions of the MedAustron Main Ring elements as well as the sequence of the elements and the initial magnet strengths are loaded into MAD-X.

2. **Loading the parameter file**: The lattice parameter (for example tune, chromaticity, strength of the resonant sextupoles and number of turns) are loaded from a file created by Python containing the values needed for the particular simulation.

3. **Adjustment of the sequence**: The loaded sequence is adjusted to fulfill the needs of the particular simulation. Marker points at the begin and the end of the electrostatic septum (ESE) as well as the betatron core unit (MIN) or the knockout exciter (KOE) are defined and installed in the lattice sequence.
   The asymmetry of the ESE is implemented by applying an offset to the aperture. This ensures that particles are extracted when their horizontal position is below -35 mm, but are lost only when they exceed a horizontal position of +70 mm.
   The width of the ESE wire (0.1 mm) is included during post-processing via Python. As the particle position is only checked at the begin of the septum, an effective width of 0.5 mm is set to mark the particles which hit the wire while passing the septum as losses. This value is a conservative approach and over-estimates the ESE losses.

4. **Matching**: The strength of the quadrupoles and the sextupoles are varied to match the desired values for tune and chromaticity.

5. **Slicing**: All components of the lattice are sliced to enable a thin tracking. Sextupoles are split into three thin slices, while quadrupoles an dipoles are treated as thick elements, as a thick map has been explicitly derived for these components. To

preserve the edge focusing effects of the dipoles, the slicing process generates dipole edge elements for them.[37]

6. **Re-matching**: After the slicing, the tune and the chromaticity have to be re-matched by varying the sextupole strengths.

7. **Tracking**: For the tracking process, the initial particle distribution is loaded from an external file. The observation point is defined as the marker at the begin of the ESE.
   A macro command allows to dynamically change parameter during tracking. The resonant sextupole is ramped from 0 to the value specified in the parameter file in the first 3000 turns. After the ramping, the parameter remain unchanged for another 500 turns. This 'rest time' is necessary to let the system stabilize to avoid unwanted effects. Finally, the betatron core (or the knockout exciter respectively) is turned on by setting the kick strength to the desired value.
   The tracking is performed for $1.5 \cdot 10^5$ turns and the losses are recorded. Every particle which is lost at the negative side of the ESE can be considered as extracted from the synchrotron.
   In addition, the position in 6D phase space of all particles are recorded turn-by-turn to plot the phase space during the extraction process.

After every change to the lattice, the lattice parameter (i.e. β, α, dispersion D and D' as well as the phase advance μ for both horizontal and vertical plane) are re-calculated using the TWISS command to track the changes in the optics. It was assured that relevant parameter are not altered too much to ensure that the found solution is not completely different to the previous one.